Response to Referee #1

We would like to thank the referee for his/her careful and thorough reading the manuscript and consider it is well written and relevant to ACP. Below are our responses to specific and technical comments.

#203 – it would be useful to outline the impact of the correction of grid cell FRP for cloud cover (i.e. the percentage FRP adjustment).

Response: We added following description:

"Cloud cover (CC) fractions in some grid cells occasionally reach 0.5 (50%), but most are zero. After the cloud cover adjustment the mean FRP areal density across the study area increased by 11.5%, so the overall effect of the CC adjustment is relatively minor."

#225 and Figure 4 – the model fits the observed Himawari FRP well for most of the diurnal cycle although there is a reasonably strong secondary peak in fire activity around 20:00 which is not modelled. What is the impact of omitting the FRP contribution of this secondary peak to the daily FRE? (i.e. the difference between the 'modelled' Himawari FRP and the observed Himawari FRP). Figure 4 shows the 'summer' diurnal cycle. Are the observed Himawari diurnal cycles similar in shape in different seasons?

Response: The reason we do not model the secondary peak in daily FRE is that there is no satellite data from VIIRS available at this time of day to influence the peak magnitude. Instead of explicitly including this peak in the modelled diurnal cycle we include an FRP baseline above a zero value that is designed to make the daily FRE the same as if the secondary peak was modelled. This "baseline" methodology follows that of Andela et al. 2015 who used it for the same reason. To address the reviewers question we designed two simulations to compare this approach (Simulation 1) to that when the secondary peak is included (Simulation 2). In Simulation 1, the FRP derived from Himawari-8 at the VIIRS daytime and nighttime overpass times are used as ρ_peak and ρ_basein, whilst in Simulation 2 the distribution shown in Fig. 4 in our manuscript (red dots) is described as the sum of two Gaussian functions:

$$\tilde{\rho}S2(t) = \sum \rho_{peaki} e^{-\frac{(h_t - h_{peaki})^2}{2\sigma_i^2}}$$

Where σ_i from each peak i in Fig. 4 (2.39±0.053 for σ_1 and 1.24±0.12 for σ_2 during June, 1.63±0.041 for σ_1 and 0.60±0.077 for σ_2 during October) are used here, h_{peaki} (h) is the hour in day when FRP reaches maximum for each of the peaks in the diurnal cycle (14.0 for h_{peak1} and 21.2 for h_{peak2} during June, 14.2 for h_{peak1} and 18.4 for h_{peak2} during October). The ρ_{peaki} are the daily Himawari-8 FRP observations at those two peak maximum times.

Results from these two simulations are shown in the Figure below, which has two time series covering 10th June to 15th June each. The upper time-series shows a comparison of the two simulations using the original FRP data from Himawari-8 and Simulation 1 (S1). S1 shows a slightly overestimated baseline on 10 June and underestimation of FRP near the second peak on 13 June. Meanwhile the lower timeseries is for Simulation 2 (S2), which shows better agreement with the original Himawari-8 FRP data on 13 June but a very slight overestimation on 11 June. However, the main purpose of including the diurnal cycle is to generate correct FRE daily values, so it is better to compare FRE totals from S1 and S2 rather than hourly FRP, and we do this in the scatterplots below.

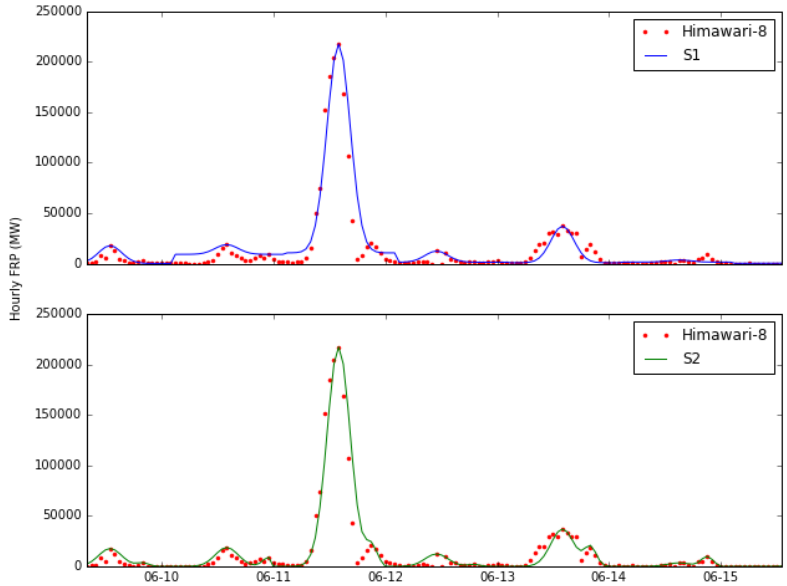

The summed daily FRP is here used to represent FRE (without the full temporal integration). The scatterplots show a direct comparison of the summed daily FRP totals from S1 (blue, left) and S2 (green, right) as compared to those from Himawari-8. Comparisons are done for Summer (June) and Autumn (Oct). The slopes of the linear best fit to these data are 1.06 and 1.15 for S1 and S2 in June, and 0.97 and 0.94 in October, suggesting that S1 performs better in both June and October. The absolute differences of S1 and S2 compared to the "true" Himawari values are however always within 10% of each other. Therefore the impact of not including the 2nd diurnal cycle peak but representing this by a baseline instead is not considered highly significant.

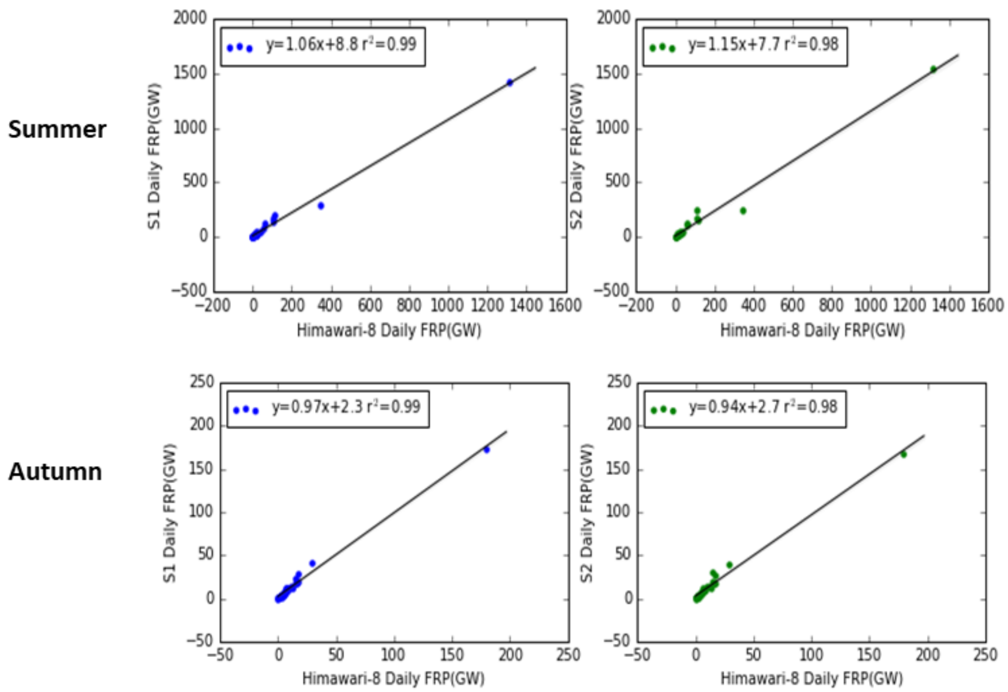

The observed Himawari diurnal cycles look indeed similar in shape in different seasons except for the autumn main peak is smaller and second peak time is earlier.

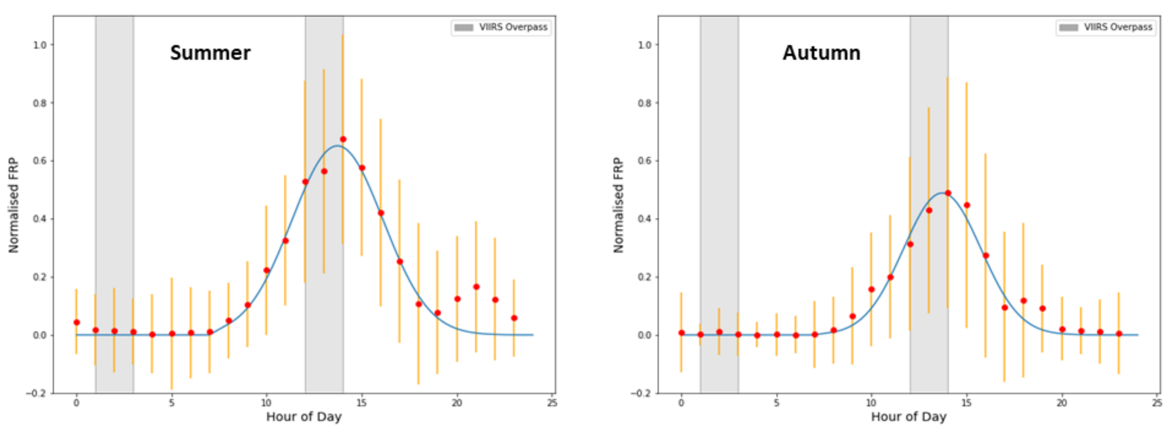

#302-310 – is the winter burning season (shown in Figure 5) detected in other emissions inventories (e.g. GFED and GFAS)? It would be useful to highlight the winter burning season in Figure 7. In relation to Figure 5, is there any difference in the proportion of day/night fire detections during the winter months?

Response: We have enhanced Figure 7 as the reviewer suggested, and we also demonstrate that this winter burning season was not detected by either GFED or GFAS.

We also investigate the day/night fire detections during summer/autumn/winter seasons and haven't observed significant difference among them. Below gives an example figure from year 2013.

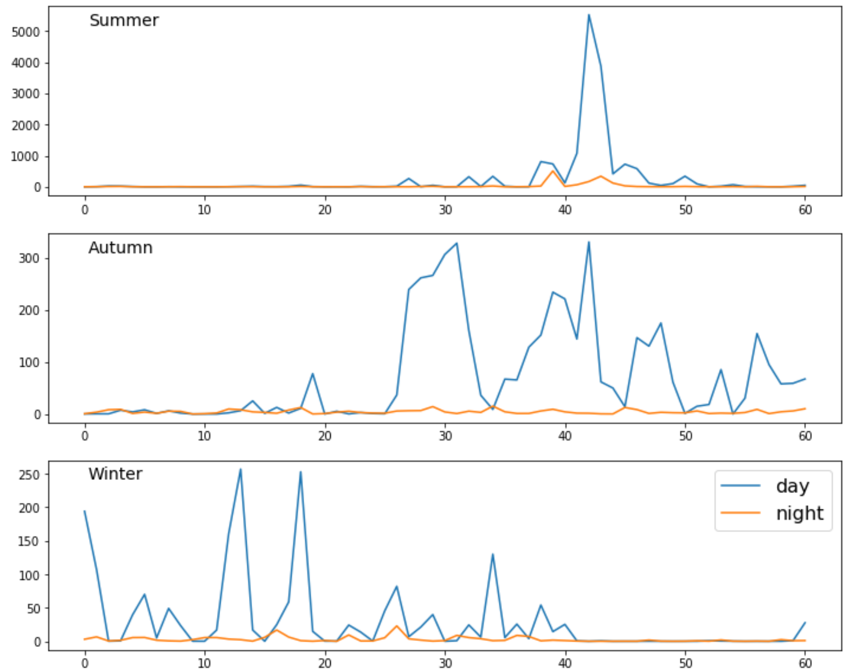

#~321 –What might be the cause in the reduction of amount of wheat residue burnt? The wheat yield in 2015 is marginally higher than it is in previous years (Table S1)?

Response: The authors believe that the most likely cause of the reduction in wheat residue burnt in 2015 compared to the prior two years is the introduction of a more aggressive policy with regards to banning agricultural residue burning. This was introduced by the local government in 2014 and was seen by us during fieldwork conducted in June 2014 and October 2015, with the latter seeing more restrictions and less burning. We also investigated yearly total FRP from MODIS Aqua in the 2003-2018 period in 30 provinces/cities (below plot). We notice that most of the provinces and cities also show this pattern of a significant reduction in burning from 2015.

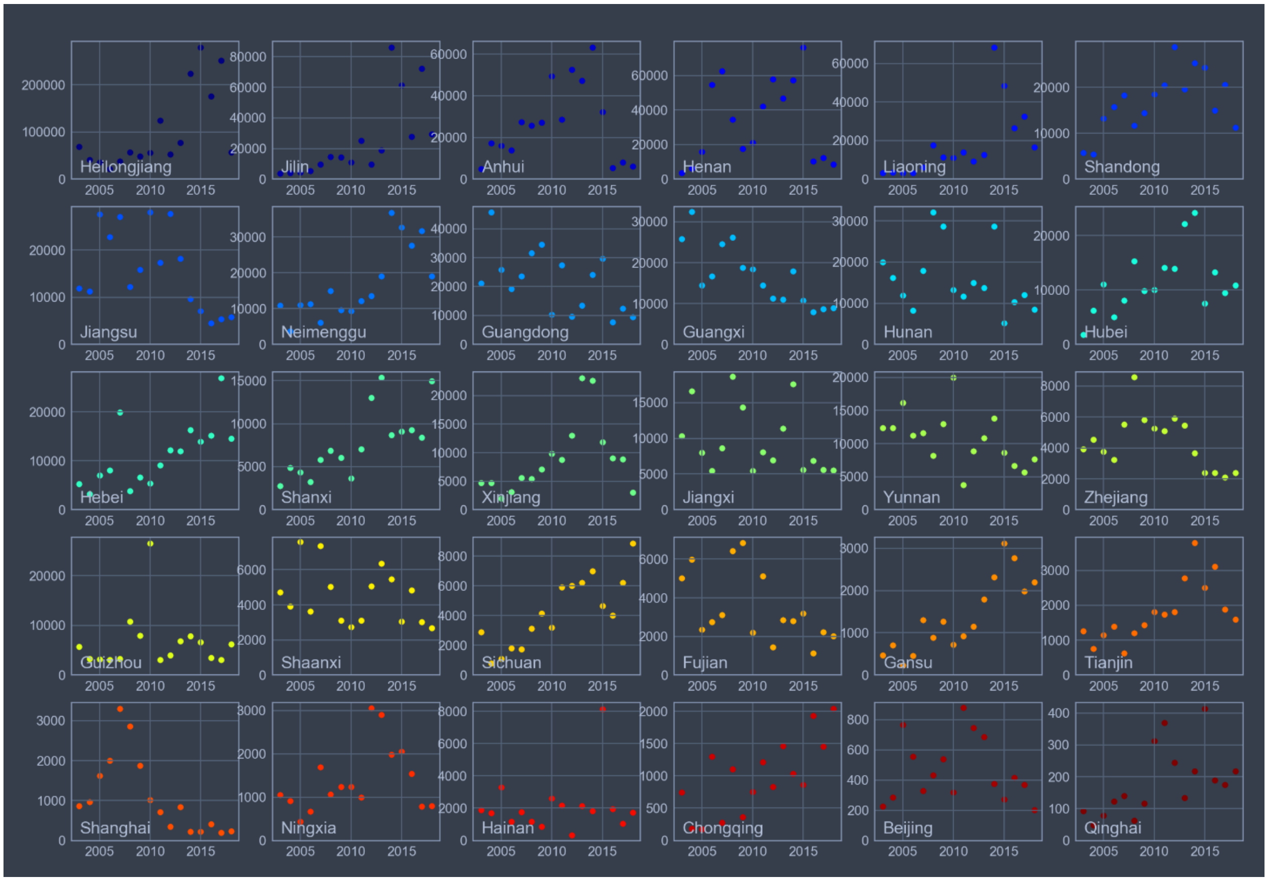

#354-359 – how do the agricultural emissions derived using this approach compare with those from Li et al., 2015

Response: The authors apologise here we used wrong citation in the manuscript, it should be the MIX inventory paper as below:

Li, M., Zhang, Q., Kurokawa, J.I., Woo, J.H., He, K.B., Lu, Z., Ohara, T., Song, Y., Streets, D.G., Carmichael, G.R. and Cheng, Y.F., 2015. MIX: a mosaic Asian anthropogenic emission inventory for the MICS-Asia and the HTAP projects. Atmos. Chem. Phys. Discuss, 15(23), pp.34813-34869.

In this paper, the authors stated that 'open biomass burning was considered as a natural emission source and excluded in the MIX inventory'. Therefore, we can only compare our emission to the listed four anthropogenic emissions in this study.

#459 – what are the combustion completeness values used in EO-derived emissions inventories such as GFED for residue burning?

Response: Leeuwen et al. (2014) was the source of combustion completeness (CC) values used within GFED. It reports that 'for crop residue CC, values ranged from 65 % for cotton and sugarcane and 85 % for wheat and bluegrass'. We use a CC value to convert our fuel consumption estimates into an estimate of the amount of dry matter that is actually set fire to in the fields. We assume a CC of what of 86% (Table

S2) based on Huang et al., 2012, which is very close to the 85% assumed in GFED. So therefore our calculated “residue amount” is given by (fuel mass burned/0.86). This then is compared to the wheat yield data to give our “burning ratios” presented in Figure 10.

#482 – Are the DMB estimates for all crop types and were these calculated using the GlobalLand30 agricultural area estimates? How do these estimates compare to those from other studies?

Response: Yes, the DMB estimates in this study are for all crop types, and they were calculated using the GlobalLand30 landcover map for agricultural areas. We used the MIRCA2000 rotation cultivation dataset to identify which crop type was burning at a particular location at different times of year (Figure S1).

Figure 7 gives comparison of DMB reported in this paper compared to that of GFAS and GFED. We have generally higher estimates than GFAS/GFED thanks to the ability of the VIIRS sensor to identify far lower FRP fires (Zhang et al., 2017). Since agricultural residue fires are typically quite small and of low intensity, this ability significantly improves the overall estimate of DMB for these types of fires. Most regional crop residue burning estimates are based on the aforementioned “bottom up” crop yield-based approach and whilst they often do not report DMB estimates they do report CO2 emission estimates which are directly proportional to DMB because CO2 represents almost 95% of the carbon released. We already compare the CO2 emissions values from our methodology to those from the “bottom up” approach in Table 2.

#56 – ‘this leads’

Response: Revised as suggested.

#63 – define MODIS

Response: Revised as suggested.

#65 – ‘most BA’

Response: Revised as suggested.

#66- define GFED

Response: Revised as suggested.

#75 - define VIIRS

Response: Revised as suggested.

#210 – replace ‘observed’ with averaged

Response: Revised as suggested.

#223 – replace ‘height’ with magnitude

Response: Revised as suggested.

#237 – replace ‘see below’ with Equation 9

Response: Revised as suggested.

#248 and 252 – replace ‘calculated’ with estimated

Response: Revised as suggested.

#466 – replace ‘most later researchers’ with ‘more recent research’

Response: Revised as suggested.

Figures

Figure 3 : Perhaps plot all of the data on the same graph and plot the data from the same day as that used in Figure 2.

Response: We have edited the plot as the referee suggests. Though the data from Himwari-8 is not available on the day used for this Figure 2 as the satellite was only launched some years later.

Figure 4 : Is the FRP diurnal cycle from all fires in Eastern China or just agricultural fires in the region?

Response: Agricultural fire is the dominant biomass burning in Eastern China, especially during burning season (accounts for over 99% of total FRP). We did include all the fires when calculating the FRP diurnal cycle. However, when we excluding those non-agricultural fires, the change to diurnal cycle is very limited. (see Figure below). We got almost similar summer diurnal cycle σ value (2.40) compare to the one we use in this paper (2.39).

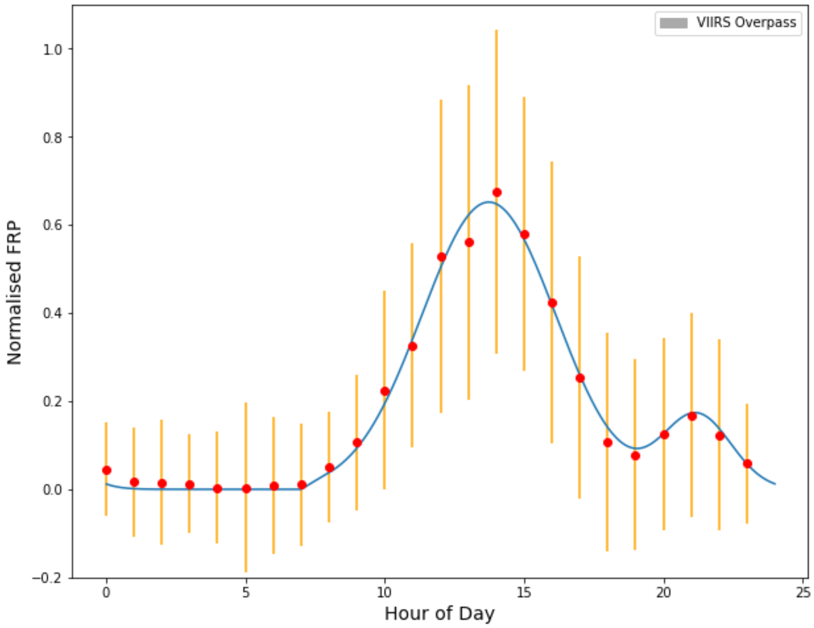

Figure 6 (and others): The density of map gridlines make it difficult to interpret the maps.

Response: We removed the gridlines and changed color theme to make the maps more readable.

Figure 8 – y-axis PM2.5 subscript

Response: Revised as suggested.

Response to Referee #2

Response: The referee has raised some concern about the issue of data aggregation to 0.1◦ resolution, which we believe we have dealt with very carefully in the paper. Below are our responses to each detailed comment provided by the referee:

(1) The authors declared that they could capture the small crop fires well happened in Eastern China, however, as we know, the fire size is often less than 100 by 100 square meters. They aggregated the fire data to 0.1◦ resolution, which is too large and not comparable with the actually existing fires. The question on small fires seem not be addressed in this manuscript.

Response:

The authors are fully aware that the Chinese agricultural lands are small and that the residue fires are also therefore small, often far less than the 100 × 100 m as the reviewer suggests. This is the reason we are using VIIRS-IM FRP data, which is based on 375 m pixels, rather than MODIS with its 1 km pixels. Active fire detection algorithms can identify fires covering only 0.0001 of a pixel area, and the smaller VIIRS pixels thus enable us to detect fires down to around 5 m^2 at night and perhaps down to around twice that by day (see Zhang et al., 2017 for details). Below we show a figure with VIIRS and MODIS fire pixel footprint sizes overlain on Google Earth for 11th June 2015 – and this highlights the advantage of the smaller pixel area of VIIRS. What we are doing is detecting the active fires at the full resolution of VIIRS, thus enabling us to capture even the small fires, and then aggregating the FRP from all of these fires detected in each 0.1-degree grid cell. So each grid cell represents the total FRP coming from all fires detected within it at the particalr overpass time.

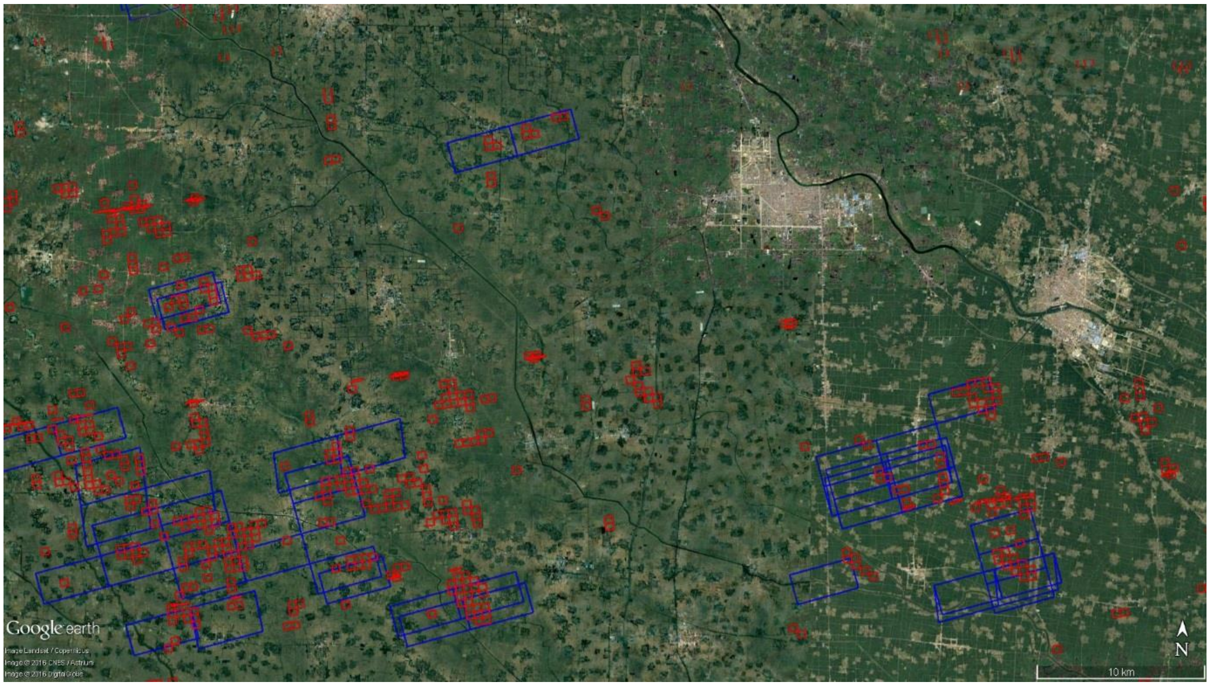

(2) Please compare your results with those from the inversions modelling or the forward simulations to check if your data are reliable. E.g., Table 2 in Cao et al. (Atmos. Chem. Phys., 18, 15017–15046, 2018), Li et al.(ATMOSPHERIC ENVIRONMENT, 92, 442-448, 2014).

The authors are struggling to compare our inventory data to Cao's et al 2018 modelling results or Li's et al. 2014 atmospheric species' concentration results. Below summarises our best effort comparison:

The measurements of NMVOC emission factors for different crop residues in China was not target for this study. To estimate NMVOC emissions, first we found GFAS uses a generic emission factor of 9.9g/kg for NMHC emitted from agricultural fires. When applying this to our data, we got an estimated yearly NMHC emission in Eastern China of 106-188 Gg in 2012-2015. Jain et al., 2014 suggested that the total emitted NMVOC from India is around 1.46 Mt while total NMHC is around 0.65 Mt. We can get a rough ratio of 2.25 for NMVOC/NMHC. If we assume Eastern China contribute a quarter of total agricultural burning to whole China, according to the publications we cited in Table 2, the total NMVOC emission is 0.96-1.69 Tg, lower but comparable to Cao et al., 2018 results of 2.08 to 3.13 (average 2.48) Tg yr^{-1} from biomass burning. It is also following our comparison in CO_2 that our values of emissions are generally smaller than results using CYBA (Crop Yield Based Approaches) method.

Li et al. 2014 only reported concentrations rather than emissions, making it even more difficult to compare. The only thing we can try here is to compare the ratio of BC/PM2.5.The average PM2.5 concentration was reported 110.7 mg/m3, containing 7.3 mg/m3 EC in their study, which accounts around 6.5% of the particle. Our yearly emission results show that around 9% particulate mass is around black carbon, slightly higher but reasonably close to Li's results. This could be because we collected our samples close to the fire, limiting the impact of aerosol aging during transportation and consequently secondary organic aerosol formation.

New eastern China agricultural burning fire emission inventory and trends analysis from combined geostationary (Himawari-8) and polar-orbiting (VIIRS-IM) fire radiative power products

Tianran Zhang[1, 2], Mark C. de Jong[1, 2], Martin J. Wooster[1, 2], Weidong Xu[1, 2], Lili Wang[3]

[1] King's College London, Department of Geography, Strand, London WC2R 2LS.
[2] NERC National Centre for Earth Observation (NCEO)
[3] LAPC, Institute of Atmospheric Physics, Chinese Academy of Sciences, Beijing 100029, PR China
Correspondence to: Tianran Zhang (tianran.zhang@kcl.ac.uk)

Abstract

Open burning of agricultural crop residues is widespread across eastern China, and during certain post-harvest periods this activity is believed to significantly influence air quality. However, the exact contribution of crop residue burning to major air quality exceedances and air quality episodes has proven difficult to quantify. Whilst highly successful in many regions, in areas dominated by agricultural burning MODIS-based fire emissions inventories such as GFAS and GFED are suspected of significantly underestimating the magnitude of biomass burning emissions due to the typically very small, but highly numerous, fires involved that are quite easily missed by coarser spatial resolution remote sensing observations. To address this issue, we here use twice daily fire radiative power (FRP) observations from the 'small fire optimised' VIIRS-IM FRP product, and combine it with fire diurnal cycle information taken from the geostationary Himawari-8 satellite. Using this we generate a unique high spatio-temporal resolution agricultural burning inventory for eastern China for the years 2012-2015, designed to fully take into account small fires well below the MODIS burned area or active fire detection limit, focusing on dry matter burned (DMB) and emissions of CO_2, CO, $PM_{2.5}$ and black carbon. We calculate DMB totals 100 to 400% higher than reported by GFAS and GFED4.1s, and quantify interesting spatial and temporal patterns previously un-noted. Wheat residue burning, primarily occurring in May-June, is responsible for more than half of the annual crop residue burning emissions of all species, whilst a secondary peak in autumn (Sept-Oct) is associated with rice and corn residue burning. We further identify a new winter (Nov-Dec) burning season, hypothesised to be caused by delays in burning driven by the stronger implementation of residue burning bans during the autumn post-harvest season. Whilst our emissions estimates are far higher than those of other satellite-based emissions inventories for the region, they are lower than estimates made using traditional 'crop yield-based approaches' (CYBA) by a factor of between 2 and 5x. We believe that this is at least in part caused by outdated and overly high burning ratios being used in the CYBA approach, leading to the

overestimation of DMB. Therefore we conclude that that satellite remote sensing approaches which adequately detect the presence of agricultural fires are a far better approach to agricultural fire emission estimation.

Keywords: Agriculture, Biomass Burning, Active Fire, VIIRS, Air Quality, Fire Emission

1. INTRODUCTION

Eastern China (111 - 123 °E, 27 – 40 °N) is home to around one third of the Chinese population and includes the area of the North China Plain and the Yangtze Plain - two of the largest agricultural zones in China (Fig. 1). Cropland covers over 1.7 million km^2 of eastern China, and the region is responsible for an estimated 25% of China's crop production, including around 51% of the national rice yield (NBSC, 2012). Large amounts of crop residue (~ 60 Tg/year including stems, stalks, straw etc) results from this agricultural production (Chen et al., 2017; Huang et al., 2012; Zhang et al., 2015), and the burning of this waste in open fields is widespread across much of eastern China (Fig. 2).

This biomass burning has both local and regional scale air quality impacts, with emissions of particulate matter (PM) of particular concern (Bond et al., 2013). The East Asian monsoon system that influences much of mainland China results in prevailing north-westerly to south-easterly atmospheric transport during winter, which is reversed in the summer months. Under these influences, the smoke from agricultural residue fires in Eastern China often affects "mega-cities" like Beijing and Shanghai (Chan & Yao, 2008; Cheng et al., 2013; Du et al., 2011; Li et al., 2010). Modelling studies show that these agricultural emissions can drive intense regional air pollution episodes; Huang et al. (2012) suggest that PM_{10} concentrations in some cities could reach 600 µg m^{-3} during such episodes, a level 6× higher than the WHO 24h-mean PM_{10} air quality guideline for human health (WHO, 2005).

Agricultural burning in eastern China accounts for a significant part of China's total biomass burning emissions (Streets et al., 2003; Chen et al., 2017), however the specific contribution of crop residue burning to air quality exceedances in China remains uncertain, partly because there is considerable doubt as to the amount of dry matter burned (DMB) in crop residue fires. For example, this leads to a ~450 % range in total crop residue burning black carbon emissions in Asia between different emissions inventories (Streets et al., 2003), while emissions estimates of gaseous species are similarly varied.

A major source of this uncertainty stems from the hitherto relatively poor ability of earth observation (EO) satellite instruments to adequately detect biomass burning activity in many agricultural areas due to the small size of the fires usually found in these areas. Many agricultural fields in eastern China are typically only around 700 m^2 in area (NBSC, 2012), and fires ignited to burn across the stubble left in the place after harvest are therefore hard to detect with moderate spatial resolution burned area (BA) mapping from sensors such as MODIS (Moderate Resolution Imaging Spectroradiometer), and are made even more elusive by the common farming practice of pilling up residues into an even smaller area before igniting them (Zhang et al., 2017; 2018). As most~~ly~~ BA mapping methods require ~ > 20 %

of a pixel to be burned in order for it to be classified as 'fire affected' (Giglio et al., 2006; 2009), BA-based emissions inventories such as GFED (Global Fire Emissions Database) tend to significantly underestimate fire activity in areas such as eastern China (Zhang et al., 2018).

Infrared based Active fire (AF) based detection techniques can discriminate fires covering only 0.01-0.1 % of a pixel area (Wooster et al., 2005; Schroeder et al., 2014), and as such should in theory be able to capture far more fire activity in agricultural areas than BA based methods. Nevertheless, due to the extremely small size of agricultural fires in eastern China, a large proportion of fire activity remains undetected by AF detection algorithms applied to 'moderate' spatial resolution imagery (from sensors such as MODIS). This limitation is a key source of uncertainty within the FRP approach, and indeed in fact can lead to biased (underestimated) FRP totals caused by the non-detection of the lower FRP component of a regions fire regime (e.g. Roberts et al., 2015). Higher spatial resolution polar-orbiting sensors such as VIIRS (Visible Infrared Imaging Radiometer Suite) can provide the ability to identify an increased number of AFs having lower FRP values, particularly when used with algorithms optimised for small fire detection (Zhang et al., 2017) (Fig. 2), but they still only capture fires burning in clear skies at the time of the satellite overpass (Giglio et al., 2003; 2006). This limitation is also a considerable source of uncertainty, and a hinderance given the sometimes short duration of active burning (especially of agricultural fires) and the typical polar orbiting imaging frequency of only a few times per day. To cope with this issue, FRP-based emissions inventories such as GFAS based upon AF methods are generally required to make assumptions or exploit additional data on the timing and relative diurnal variability of fire activity occurring between polar orbiting overpasses in order to estimate, for example, total daily Fire Radiative Energy (FRE) (Kaiser et al., 2012; Xu et al., 2017; Zhang et al., 2017). Here we provide this additional information by exploiting new fire diurnal cycle information taken from the geostationary satellite Himawari-8, combining it with twice daily FRP information provided by the 'small fire optimised' VIIRS-IM product of Zhang et al. (2017) to produce a unique high spatio-temporal resolution agricultural fire dataset (referred to hereafter as the VIIRS-IM/Him dataset) for eastern China based on FRE totals. This new inventory is designed to reduce bias and uncertainty caused by use of one FRP data type alone, and to account for small fires burning even for short periods and often well below the MODIS AF and BA detection limit. The fuel for these fires is waste straw and other agricultural residues, and we use a crop rotation map to classify the type of agricultural residue being burned at each observed location and time. It is then used to select the most appropriate smoke emissions factor for calculating the final fire emissions totals from FRE derived estimates of dry matter burned (DMB).

2. DATASETS

2.1 Polar Orbiting VIIRS-IM FRP Product

The Visible Infrared Imaging Radiometer Suite (VIIRS) instrument is currently flown aboard the polar orbiting Suomi NPP (since 2011) and NOAA-20 (since 2017) satellites and expands upon the capabilities of the AVHRR and MODIS instruments for environmental monitoring (Zhou et al., 2019). VIIRS has 22 channels spanning the visible to the longwave infrared, a 3000 km swath width, and nadir pixel resolution ranging between 375 m and 750 m (Goldberg et al., 2013). Furthermore, a ‘pixel aggregation’ scheme is applied to VIIRS which limits pixel area increase with scan angle to a maximum of 4× compared to MODIS' 10× (Wolfe et al., 2013).

With a necessary emphasis on the detection of small fires typical of agricultural regions, our work focuses on generating a gridded daily biomass burning fuel consumption product that estimates DMB and emissions from the VIIRS-IM AF Detection and FRP product developed and optimised for eastern China by Zhang et al. (2017), using data from the instrument aboard the Suomi NPP satellite with a mean local daytime overpass time of 13:30 in the ascending node, and a mean local nighttime overpass time of 01:30 in the descending node (Wolfe et al., 2013). Fig. 2 shows an example of the VIIRS-IM FRP product, generated from the two observations per day provided by Suomi NPP VIIRS. This FRP product blends the advantages of the ‘small fire’ sensitivity of the VIIRS 375 m I-Band, with the ability to retrieve fire radiative power (FRP) over larger fires using the 750 m M-Band observations. Due to the very small size of agricultural fires in China, and because the VIIRS I-Band pixel area is 10× smaller than the pixel area of MODIS, far more fires can be detected in eastern china using the VIIRS-IM AF product of Zhang et al. (2017) than can be identified in near simultaneous MODIS data, and on average across eastern China retrieves FRP totals around 4× higher (Zhang *et al.*, 2017).

2.2 Geostationary Himawari FRP Product

To convert the twice-daily VIIRS-IM FRP product to daily-integrated FRE, information on the fire diurnal cycle is required (Ellicott et al., 2009; Freeborn et al., 2008; Roberts et al., 2009). We obtained this from 10-min temporal resolution observations from the geostationary Himawari-8 satellite, whose data have recently been used to derive AF detections and FRP metrics across Asia by Xu et al. (2017). Himawari cannot be used in isolation to directly estimate daily FRE for each of the 4-years of the study, because (i) Himawari data are only available from early 2015 onwards, and (ii) Himawari’s relatively coarse pixel size (2 km at the sub-satellite point) means that it omits even more of the agricultural fires than does MODIS (as illustrated by Xu et al., 2017 and in Fig.3). However, where agricultural fires are concentrated in sufficient density, observations by Himawari do enable their detection and these data can be used to map the changing FRP of these fires over the day for derivation of the fire diurnal cycle.

2.3 Crop Rotation Map

The predominant agricultural residues burned across eastern China are wheat, corn and rice straw (Huang et al., 2012). To classify the likely residue type of each detected fire, a crop rotation map (Fig. S1) was generated from the MIRCA2000 0.08º global monthly crop area dataset (Portmann *et al.*, 2010), which has a spatial resolution equivalent to 9.2 km $\times$ 9.2 km at the equator. These data were used to assign fire activity to a particular crop residue type, which determined the appropriate agricultural biomass burning emission factors to apply (see Section 3.3).

2.4 Land Cover Data

We use the GlobeLand30 land cover product (Chen et al, 2015) to classify land cover/use for our study area in Eastern China. GlobeLand30 provides 30m spatial resolution land cover data for a baseline year of 2010 derived primarily from Landsat (TM5 & ETM +) and China Environmental Disaster Alleviation Satellite (HJ-1) imagers. Fig. 1 shows the spatial distribution of the agricultural land ratio (regridded to 0.01 degree spatial resolution) calculated use this dataset in eastern China.

2.5 GFED & GFAS Emissions Inventory Data

The results from the combined VIIRS-IM and Himawari FRP based emissions (VIIRS-IM/Him) dataset were compared to two state-of-the-art global fire emission databases, the Global Fire Emissions Database (GFED) and the Global Fire Assimilation System (GFAS). GFED was built to combine remotely sensed data on BA with fuel loads from the CASA biogeochemical model of vegetation growth, producing monthly, spatially explicit pyrogenic fuel consumption, carbon, GHG and air pollution emission estimates at 0.25º grid cell resolution globally (Van der Werf et al., 2010; Giglio et al., 2013). The most recent version (GFED4.1s) includes a "small fire boost" based on AF detections, in an attempt to counteract the inability of the MODIS BA product to detect many agricultural fires (Randerson et al., 2012; Van der Werf et al., 2017). Due to this 'boost' GFED4.1s shows higher values of dry matter burned (DMB) in most eastern China grid cells compared to the 'unboosted' GFED4, and a more extensive fire distribution. However, Zhang et al. (2018) show that the boosting procedure can introduce significant anomalies into the GFED dataset at certain times of year, generated when MODIS' AF detection procedure incorrectly identifies urban features in eastern China as fires.

In contrast to GFED, the GFAS fire emissions database is based on AF detections and is integrated into Copernicus Atmosphere Monitoring Service (CAMS) system for near-real-time atmospheric composition monitoring and forecasting. Developed by Kaiser et al. (2012) and based on the FRP method, MODIS supplies the FRP data for the current GFAS v1.2 up to 4 times per day at most latitudes. From these observations, DMB is calculated via a regression against GFED DMB values (Kaiser et al., 2012) and daily emissions of 40 emitted species are then calculated at 0.1º spatial resolution.

2.6 Crop Yield Based Approach Emissions Inventory Data

The traditional method for estimation of agricultural fire emissions is the so-called crop yield based approach (CYBA), and we compare data from such approaches to our new VIIRS-IM/Him methodology. CYBAs typically calculate the amount of crop residue burned in a region using a combination of crop production statistics and related additional parameters using following equation:

$$DMB = \sum_{i=1}^{n} P_i R_i B_i C \qquad (1)$$

Where i stands for each of n different crops; *DMB* is total dry matter burned (kg) in the region; P_i is the regional production of crop i (kg), and is usually derived from annual agricultural statics reports; R_i is the dry matter production-to-residue ratio (unitless), which depends on the crop type i; B_i is the proportion of residue burned in the field for crop type i in the region under study (i.e. the 'burning ratio'; 0-1, unitless); and C is crop combustion completeness (0-1, unitless, Huang *et al.*, 2012). DMB is then multiplied by appropriate particulate/gaseous emission factors in order to estimate the total emissions from agricultural burning.

Certain of the parameters of Eqn. 1 are not so easily determined. For example, the burning ratio (B_i) is often based on questionnaires or investigations on the use of crop residues conducted with farmers (Gao *et al.*, 2002; Wang and Zhang, 2008). Because of strong variations in socio-economic development across the huge expanse of mainland China, large differences in the estimates of B_i exist (Jiang *et al.*, 2012; Liu *et al.*, 2008; Yamaji *et al.*, 2010). B_i may also change considerably from year to year since it is strongly impacted by the level of local economic development, the availability of alternative uses for crop residues in the region, and the regional governance of fire prohibition (Chen *et al.*, 2017). Moreover, considering the official prohibition of open air burning, the reliability of data based on surveys that ask farmer how much residue they burn is questionable. Despite this, most studies that include estimation of agricultural fire emissions in Eastern China have relied on the CYBA (e.g. Cao *et al.*, 2006; He *et al.*, 2011; Huang *et al.*, 2012; Li *et al.*, 2009; Qin and Xie, 2011; Yan *et al.*, 2006; Zhao *et al.*, 2015).

3. METHODOLOGY

3.1 Data Gridding and Cloud Cover Adjustment

The VIIRS-IM FRP product data (in MW), originally derived at the pixel scale, were aggregated to 0.1° resolution for this analysis. Unlike the daily average MODIS FRP calculation of GFAS, which weights individually contributing MODIS FRP observations by their view zenith angle to downgrade the importance of far off-nadir measurements (Kaiser *et al.*, 2012), no such weighting was applied to the VIIRS-IM FRP data since they have already shown very limited view zenith angle dependence as a result of the VIIRS' pixel-averaging procedure (Zhang et al., 2017). For each VIIRS overpass, the total observed FRP present in each 0.1° grid cell j (i.e. FRP_j) was calculated from the cumulative FRP of all native resolution AF pixels i within the grid cell:

$$FRP_j = \sum_{i \in j} FRP_i \qquad (2)$$

Total observed agricultural area (A, excluding cloud covered area) within each 0.1° grid cell was calculated similarly using the GlobeLand30 30m landcover map:

$$A_j = \sum_{i \in j} A_i \quad (3)$$

The VIIRS-IM product is only affected to a limited degree by smoke because of the relative transparency of smoke plumes at Mid-Wave Infrared (MWIR) ~~–~~wavelengths due to the dominant particle size being smaller than the wavelengths of the VIIRS MWIR channel (Zhang et al., 2017). However, the product cannot provide information in cloud covered areas, and so an adjustment is required to take into account actively burning fires hidden from view by clouds. Following Streets *et al.* (2003) we assume that for partially cloud covered grid cells, the AF and FRP distribution under cloud is the same as under the clear sky areas, as is also assumed in GFAS (Kaiser *et al*., 2012).

Subsequently, the gridded and cloud-adjusted FRP areal density (ρ_j, MW.km^{-2}) is calculated using:

$$\rho_j = \frac{FRP_j}{A_j} \quad (4)$$

Cloud cover (CC) fractions in some grid cells occasionally reach 0.5 (50%), but most are zero. After the cloud cover adjustment, the mean FRP areal density across the study area increased by 11.5%, so the overall effect of the CC adjustment is relatively minor.

Formatted: Font: Not Italic

Formatted: Font: Not Italic

3.2 Diurnal Cycle and Daily FRE Generation

Hourly averages of the 10-minute FRP data from the Himawari-8 FRP product of Xu *et al.* (2017) were gridded to the same 0.1° grid cell resolution as the VIIRS-IM dataset. For each grid cell and calendar day, hourly FRP data were normalised in order to minimise the impact of day-to-day variations in fire activity:

$$\widetilde{FRP_{j,d}^{h}} = \frac{FRP_{j,d}^{h} - \min(FRP_{j,d})}{\max(FRP_{j,d}) - \min(FRP_{j,d})} \quad (5)$$

Where $\widetilde{FRP_{j,d}^{h}}$ is the normalised Himawari-8 FRP for hour *h* on day *d* for grid cell *j*; $FRP_{j,d}^{h}$ is the ~~observed~~ averaged Himawari-8 FRP (MW) for hour *h* on day *d* for grid cell *j*; $\max(FRP_{j,d})$ and $\min(FRP_{j,d})$ are respectively the maximum and minimum hourly Himawari-8 FRP (MW) observed on day *d* for grid cell *j*. Note that *h* is in local time (UTC/GMT + 8 hours) and the diurnal cycle runs from 0 to 23 hours.

$\widetilde{FRP_{j,d}^{h}}$ data for 2015 were used to produce two normalised 'seasonal' diurnal fire cycles for the eastern China study area: a 'summer' diurnal cycle, constructed from May-June data, and an 'autumn' diurnal cycle, constructed from Sept-Oct data. Both normalised seasonal diurnal cycles were calculated using a weighted mean so that days and grid cells with high fire activity had the greatest influence on the cycle:

$$FRP^{h} = \frac{\sum_d \sum_j \left(\widetilde{FRP_{j,d}^{h}} \times FRP_{j,d}^{h}\right)}{\sum_d \sum_j \left(FRP_{j,d}^{h}\right)} \quad (7)$$

Where FRP^h is the normalised FRP for hour h for the entire study area and fire season (summer or autumn). Fig. 4 shows the resulting weighted mean fire diurnal cycle for the summer season for Eastern China. This diurnal cycle is bi-modal: a primary peak occurs around 13:00 local time that extends from around 08:00 to 18:00 (daytime) and a second much smaller peak occurs around 21:00 local time (with a magnitude ~~height~~ of only ~ 20% of the normalised FRP value of the first peak).

We blended information from the Himawari FRP diurnal cycle with the instantaneous twice-daily VIIRS-IM FRP areal density (ρ_j, $MW.km^{-2}$) data, using an approach based on Andela et al. (2015) to create the VIIRS-IM/Him dataset. Here we represent the diurnal fire cycle as a gaussian function parameterised using the Himawari FRP diurnal cycle, superimposed on a fixed baseline. For a given grid cell *j*, at instantaneous time *t*, VIIRS-IM/Him FRP areal density is calculated by:

$$\rho_{VIIRS-Him_{j,t}} = \rho_{VIIRS_{night,j}} + \mu\left(\rho_{VIIRS_{day,j}} - \rho_{VIIRS_{night,j}}\right) e^{-\frac{\left(t - t_{Himpeak}\right)^2}{2\sigma^2}} \quad (8)$$

Where $\rho_{VIIRS-Him_{j,t}}$ is the instantaneous VIIRS-IM/Him FRP areal density ($MW.km^{-2}$) for grid cell *j* at time *t*; $\rho_{VIIRS_{night,j}}$ is the night-time (~01:00 LST) VIIRS-IM FRP areal density value ($MW.km^{-2}$) for grid cell *j*; $\rho_{VIIRS_{day,j}}$ is the day time (~13:00 LST) VIIRS-IM FRP areal density value ($MW.km^{-2}$) for grid cell *j*; μ is an adjustment factor used to account for the difference between the VIIRS daytime overpass time and the peak time of the weighted mean fire diurnal cycle (Eqn. 9~~see below~~); $t_{Himpeak}$ is the time of day at which the seasonal Himawari FRP diurnal cycle peaks; σ is the standard deviation of the main peak of the Himawari FRP diurnal cycle, calculated by fitting a gaussian function (using non-linear least squares) to the seasonal Himawari FRP diurnal cycles. The summer diurnal cycle σ value (2.39±0.053) was applied during the April-August period, and the autumn diurnal cycle σ value (1.63±0.041) was applied during the September-March period.

The adjustment factor μ is used to account for the fact that the VIIRS daytime overpass time is unlikely to coincide with the peak of the fire diurnal cycle:

$$\mu = e^{\frac{\left(t_{VIIRS_{day,j}} - t_{Himpeak}\right)^2}{2\sigma^2}} \quad (9)$$

Where $t_{VIIRS_{day,j}}$ is the local time of the VIIRS-IM FRP observation for grid cell *j*.

Daily FRE was then estimated ~~calculated~~ for each grid cell j and calendar day by integrating the instantaneous VIIRS-IM/Him FRP data using Eqn. 8.

3.3 Conversion to Dry Matter Burned (DMB) and Smoke Emissions

To convert the estimated ~~calculated~~ FRE areal density to fuel consumption/DMB, we multiplied FRE by the 0.368 (±0.015) $kg.MJ^{-1}$ factor derived by Wooster *et al*. (2005) from a series of outdoor experimental straw fires, that were very similar to the Chinese agricultural residue fires used herein (Zhang et al., 2015). To convert the resultant DMB into smoke emissions, we used the emission factors of wheat and rice derived from *in situ* measurements in agricultural areas by Zhang et al. (2015) (Table 1). Corn residue was not a fuel type measured during those experiments, and so for this fuel type (which was only 16-22% of the total agricultural fuel consumption) we used the emissions factors for agricultural corn fires from Andreae and Merlet (2001), as is used in GFAS (Kaiser *et al.*, 2012) (Table 1). Together with the crop rotation map (see Section 2.3 and Fig. S1) the EFs from Table 1 enabled us to select the appropriate emissions factor for use at a particular location and time of year.

Furthermore, a winter burning season was discovered during November and December (see details in Section 5.1) when no cultivation crop is shown in the MIRCA2000 data in the study region. Analysis in this study shows that winter fires are likely to result from the combustion of stored residues from the autumn harvest season, therefore all fire activity in winter was assigned to crop types (and therefore emission factors) using the crop rotation map from the previous closest month (October) (Fig. S1). This methodological change is accounted for in the data presented in Fig. 5.

4. BIOMASS BURNING AND EMISSIONS RESULTS

4.1 Temporal and Spatial Distribution of FRE In Eastern China

Fig. 5 shows the time series of daily mean FRE areal density in eastern China from February 2012 to December 2015, reported at 0.1° grid cell resolution, and broken down into three main crop residue types. A strong seasonal variation is seen, with peak activity in summer (May-June) associated with wheat residue burning and a smaller secondary peak in activity occurring in autumn (Sept-Oct) associated with corn and rice residue burning. In fact, the secondary peak is a combination of several fluctuations lasting from October until December, further discussed in Section 5.1. Over the whole 4-year period, wheat crop residues contributed 65% of the total FRE, rice residues 18%, and corn residues 17%.

A distinct spatial pattern showing two main burning seasons can also been seen when FRE areal density is mapped (Fig. 6). During the summer burning season (May-June), most fires are located between 32° N - 36° N, extending from 112° E - 120° E near the coast. In the autumn season (Sept-Oct), less fire activity occurs than in the summer fire season and it is more evenly distributed across the entire study area, though there is still a focus of fire activity between 32 - 34° N and 112 - 119° E. Moreover, in the southwest of the study area (29 - 32° N and 112 - 114° E) we see a region that only appears to undergo substantial burning in the autumn. This is located in the centre of Hubei Province, which contributes around 12% of the total rice yield of the whole of China (NBSC, 2015). This area contributes to between 10 and 18 % (year dependant) of the total autumn burning season FRE.

4.2 DMB Comparisons to GFAS and GFED

The outputs generated by our combined VIIRS and Himawari processing chain were compared to those of GFAS and GFED4.1s (Fig. 7). Dry matter burned (DMB) was used as the common comparison metric, as this removes differences arising from the use of different emissions factors within the inventories. Overall, the VIIRS-IM/Him DMB estimates are around 2× to 5× higher than those reported for corresponding months by GFAS and GFED 4.1s. As detailed in Zhang et al. (2017) and discussed in Section 2, VIIRS has the ability to detect far smaller (and lower FRP) fires than MODIS, due to its far smaller pixel size and the fact that the I-band observations also retain their pixel area more effectively across the swath. Ultimately, this difference results in far higher DMB being obtained by the VIIRS-IM/Him inventory compared to the MODIS based GFAS and GFED inventories.

During the summer months of May-June, all three inventories (GFAS, GFED and VIIRS-IM/Himawari) show a clear peak in DMB, but GFAS and VIIRS-IM/Him show a much sharper peak in June, while GFED's summer burning season extends one month earlier (May) and later (July). This extended summer fire season reported by GFED is likely the result false fire reporting, discussed at length in Zhang et al (2018). VIIRS-IM/Him shows a June DMB peak ranging from 3.30 to 11.2 Tg, 2× higher than GFED4.1s (1.89 - 5.34 Tg) and GFAS (2.00 to 4.30 Tg). It should be remembered that the conversion of daily average FRP to DMB in GFAS is derived via a calibration to GFED4.1s (Kaiser *et al.*, 2012), so these two emissions databases understandably report similar monthly DMB totals.

For the autumn (Sept-Oct) burning season, the peaks in the GFAS and GFED inventories are much less pronounced than the summer burning season peaks (Fig. 7). DMB in October ranges from 0.57 - 1.74 Tg for GFED, significantly higher than the 0.31 - 0.61 Tg reported by GFAS, but far lower than the 1.62 - 3.05 Tg of the VIIRS-IM/Him inventory. The VIIRS-IM/Him derived DMB estimates for eastern China are thus 2 to 3× higher than GFED4.1s and 5× higher than GFAS; these represent larger differences than exist for the earlier summer burning season. This indicates that agricultural fires burning during the autumn fire season may be on average smaller and/or more isolated from other fires than they are in the summer burning season, and thus are even more likely to be missed by the MODIS AF detection product (Giglio *et al.*, 2006) and/or the MODIS BA product (Giglio *et al.*, 2013) than they are during other more intense burning periods.

4.3 Agricultural Fire Emissions Intercomparison

This section presents a comparison of the total annual agricultural fire emissions calculated using the VIIRS-IM/Him method with other inventories of Chinese agricultural fire emissions in the literature, and against emissions totals from other sectors to gain a better understanding of the relative importance of agricultural fire emissions. To compare with other reported agricultural fire emission inventories for China, the DMB estimates produced herein were converted to fire emissions estimates using the emissions factors and methods described in Section 3.3; these results are summarised in Fig. 8 and Table 2.

From Fig. 8, it is clear that wheat residue burning is the primary agricultural emission source, accounting for over 50% of the total emissions released each year (specifically 55-69% of $PM_{2.5}$, 71-81% of BC, 66-77% of CO_2, and 69-80% of CO). Fig. 8 also indicates a considerable reduction in emissions in 2015 compared to previous years, largely attributable to a reduction in the amount of wheat residue burnt. For example, total $PM_{2.5}$ emissions from agricultural residue burning in eastern China for 2012-14 cover a relatively narrow range of 107 - 130 Gg (Fig. 8 & Table 2), but decrease to 67 ± 24 Gg in 2015 due to an almost halving of DMB (Fig. 7); similar patterns are observed for BC, CO_2, and CO (Fig.8).

From Table 2, it is apparent that emissions totals calculated using the VIIRS-IM/Him approach are consistently higher than those reported by GFAS by factor of 1.2-4.2 (species/year dependent). Similarly, VIIRS-IM/Him emissions totals for CO_2 and PM2.5 are greater than those reported by GFED by a factor of 1.1-1.7. In both cases, this can be explained by the tendency of MODIS to miss activity from small fires compared to VIIRS. VIIRS-IM/Him emissions for CO and BC in 2015 are lower than those reported for GFED, which can be attributed to differences in the emissions factors used between the approaches.

Emissions totals calculated using the VIIRS-IM/Him approach are smaller than those estimated by CYBA studies for the East China/North China Plain regions (Zhang et al., 2008; Huang et al., 2012; Qiu et al., 2016) by a factor of 2-5. It is possible that the much higher totals estimated from the CYBA based studies maybe due to the use of very high residue burning ratios (B_i in Eq. 1) for corn and rice in particular. This finding is discussed further in Section 5.

Liu *et al.*, (2015) estimated total emissions in the North China Plain region (a similar area to the study area used in this paper) using MODIS FRP-based calculations, and assumed a modified Gaussian function for the diurnal cycle to generate the daily FRE estimates from which emissions were then derived. These estimates are much closer in magnitude to the equivalent estimates calculated using the VIIRS-IM/Him method than those from the CYBA studies, however 2013 & 2014 estimates by Liu et al. are consistently lower (by a factor of 0.3-0.9); again, we attribute this difference to the fact that MODIS based methods capture less fire activity than our VIIRS-IM/Him approach. Interestingly, Liu *et al.* (2015) estimated far higher emission totals for 2012 compared to 2013 & 2014 and report greater total CO and BC emissions than we do. For example, annual CO_2 emissions in 2012 (26,000 Gg) are > 2× their reported total emissions for 2013 (9800 Gg) and 2014 (13,000 Gg). However, Liu *et al.*'s processing approach did not provide any adjustment for the impact of the MODIS 'bow-tie' scan geometry effect, which leads to duplicated AF detections and this FRP towards the edge of the MODIS swath, and which was highlighted as significant issue for FRP quantification by Freeborn *et al.* (2008) and Zhang et al. (2017). This is a particular problem in MODIS data from the year 2012, where large amount of duplicated observations have been found towards edge of swath (Fig. S2). This problem has been addressed in GFAS using a scan-angle dependent weighing factor for the MODIS FRP data

(Kaiser *et al.*, 2012), as described in Section 2.5, and GFAS' CO_2 emissions from 2012 are only 24% and 10% higher than from 2013 and 2014 respectively, a much more modest increase compared to that reported in Liu *et al.* (2015).

Fig. 9 presents a comparison of agricultural emissions calculated using the VIIRS-IM/Him method with emissions from non-biomass burning sources produced by Li et al. (2014) for a sub-area of eastern China (32-36º N, 112-122º E) for the year 2013. We note that crop burning emissions are of relatively little significance when considered on an annual basis; for all four species (CO_2, CO, $PM_{2.5}$, BC), contributions from agricultural residue burning range between 0.56% and 2.0% of total annual emissions, with the majority of emissions resulting from industry and residential sources. However, in June when agricultural burning and emissions are at a maximum, residue burning contributes 8.1%, 18%, 22% and 20% of total monthly emissions for CO_2, CO, $PM_{2.5}$ and BC respectively, highlighting the strong seasonal impact agricultural burning can have on the emission of species that affect both climate and air quality.

5. ANALYSIS AND DISCUSSION

5.1 Importance of Wheat Residue Burning

Findings in Section 4 (Fig. 5 & 8) indicate that a larger proportion of wheat residue than corn or rice residue is burnt, for several reasons. First, the yields of these three crop types in Eastern China are relatively similar - in 2015 for example, wheat yield was 10% lower than rice yield, and only 20% higher than corn (Table S1; NBSC, 2015). Second, the dry matter production-to-residue ratio (R_i in Eqn. 1) of wheat is not higher than that of rice or corn (Table S2; Wang and Zhang, 2008). Third, with the exception of black carbon, the emission factors for wheat residues are broadly similar to or smaller than the corresponding rice and corn emission factors. It is unknown why a greater fraction of wheat residue than corn and rice residue is burnt, however, it is possible that local management practices and/or stakeholder priorities differ depending upon the residue type and time of year at which crops are harvested, ultimately impacting the fate of these residues e.g. residues from certain crops maybe valuable as fertiliser (Huang et al., 2012), animal feed or for domestic/local energy production (Chen et al., 2017; Liu et al., 2008).

5.2 Discovery of A Winter Burning Season

As detailed in Section 4.1, small peaks in our dry matter burned (DMB) time-series are apparent in November-December of each year (grey shaded area shown in Fig. 5). Since no mention of such a winter burning season was found in the literature (e.g. Chen *et al.*, 2017; Huang *et al.*, 2012; Zhang *et al.*, 2008), these winter peaks were initially considered to be erroneous and likely caused by VIIRS AF false alarms that had failed to be excluded by the landcover and/or persistent thermal anomaly masking detailed in Zhang et al., (2017). Furthermore, according to the crop rotation map derived from the MIRCA2000 data (Fig. S1), there is no obvious harvesting of wheat, corn, or rice during the winter in eastern China. However, close examination of the original VIIRS data and the VIIRS-IM FRP product generated from it by Zhang et al., (2017) shows that most of the AF pixels detected in eastern China in winter are in fact located in or very close to areas classified as agricultural land (Fig. S3), and are not located close to industrial areas of the type known to cause false AF detections (Zhang et al., 2017), nor do the AF detections appear multiple times in the same month at the same location, as would be expected if they were false alarms generated by non-fire features. It therefore seems highly probable that these AF detections are actually a consequence of true agricultural burning (Fig. S3-5).

The most reasonable explanation for the winter AFs appears to be that some of the crop residues from the Sept-Oct (Autumn) harvest season were left idle for a few months and burned in the winter, rather than immediately. Local newspapers, online media and other information sources were consulted, and were found to support the existence of winter residue burning episodes. One example is a report by Jiangsu Province TV station in 5 December 2013, where a huge crop residue burning episode was reported in Hongze (Jiangsu Province), close to the location shown in Fig. S3. Stills from this TV report show flames, thick smoke and extremely poor visibility resulting from the crop residue burning, described in Chinese language subtitles (Fig. S4). Reports of similar episodes were found in different websites/newspapers from across much of eastern China (e.g. Wang and Zhang, 2016; Za, 2015; Zuo, 2015). Subsequent to this confirmation, an explanation as to why this activity may have occurred outside of the normal burning season was sought. According to Yun Xia, a local governor of the Environmental Department in Hefei (interview conducted by Anhui News; Zuo, 2015), the prohibition on agricultural burning started at beginning of September in that area, and continued up until the 20th November. During this period, the local government strongly enforced its polices aiming to restrict agricultural residue burning, and established almost continuous patrols to identify areas likely to host crop residue fires in order to prevent their ignition. However, without a widespread and cost-effective alternative way to dispose of their crop residues, local farmers may simply have stored the residue material and burned it soon after the end of the prohibition period, when the intensive patrol period had ceased. The end of the prohibition period coincides almost exactly with the time of the new winter burning season identified by our VIIRS-IM/Him dataset (Figs. 5- 7).

The winter season is important for biomass burning in this area of China, accounting for between 19 and 36 % (year dependant) of the combined autumn and winter FRE total. Based on the crop rotation map (Fig S1), this fire activity was assigned to the burning of both corn and rice residues, with the contribution of each residue to total FRE (and thus DMB) almost equal (49 % and 51 %, average over all years). This split by residue type is very similar to that observed in the Autumn burning season (corn = 54 %, rice = 46 %, average over all years), despite the observed variation in the spatial distribution of fire between autumn and winter (Fig. 6). In general, winter burning appears to take place closer to provincial capitals than autumn burning does; the reason for this spatial shift in fire is discussed in Section 5.4.

5.3 Disagreement Between Satellite Derived Emissions and Crop Yield Based Approaches

In Section 4.3, it was noted that annual emissions totals calculated using crop yield based approaches (CYBAs) are greater than those calculated using the VIIRS-IM/Him method by a factor of 2-3, depending on species. We believe that this discrepancy relates to the ‘burning ratio’ (BR) used in CYBA to produce emissions estimates. The burning ratio is the ratio of crop residue burned in the field compared to the total amount of residue produced by harvesting, and is a key parameter in bottom up CYBAs (see Eqn. 1, and Chen *et al.,* 2017; Gao *et al.,* 2002; Huang *et al.,* 2012; Li *et al.,* 2016). Streets *et al.* (2003) used a uniform BR of 17 % derived from 1970's data, however more recent studies often make use of regionally varying fractions. We identified three sources of regionally varying burning ratios that are widely used in the CYBA literature:

i) Wang and Zhang (2008), divided all provinces in China into six zones according to their geographical distribution. A questionnaire-based survey conducted amongst farmers within these regions was used to elucidate the level of burning activity, and using the responses it was determined that burning ratios for the different categories ranged from 11% to 33%. Outputs were applied and referenced in a series of fire emission studies (He *et al.,* 2011, Qin and Xie 2011, Zhang *et al.,* 2016).

ii) Gao *et al.* (2002) derived a set of province-dependent burning ratios adopted from a large-scale investigation of crop residue use across different Chinese provinces. These ratios have been used and referenced in Huang *et al*. (2012), Yan *et al*. (2006), Zhang *et al*. (2008), and are shown in Fig. 10.

iii) A derived value based on farmers' income levels, based on the fact that Cao *et al.,* (2006) found a positive linear correlation between the income of farmers and burning ratio (r = 0.81). This relationship has been applied within several fire emission studies (Sun *et al.,* 2016, Zhao *et al.,* 2015) and will be examined in Section 5.4.

Using crop yield information and the DMB data derived from the VIIRS-IM/Him processing performed herein, it is straight forward to reverse the CYBA methodology to calculate the burning ratio for each crop type. This procedure can help confirm whether the outputs derived herein are comparable with those of the existing literature, as well as enabling the advantages offered by the remote sensing time series to be fully exploited. The burning ratios (B_{ij}) for each province *i* and crop type *j* are calculated from:

$$B_{ij} = \frac{DMB_{ij}}{P_{ij}R_iC} \tag{10}$$

Where DMB_{ij} is the estimated VIIRS DMB (g/m^2) for province *j* and crop *i*; P_{ij} is the yield of crop *i* for province *j* (kg); R_i is the dry matter production-to-residue ratio for crop *i* (unitless) and *C* is crop combustion completeness (proportion, 0-1). The province level crop yield P_{ij} is derived from annually published statistical reports, and are presented in Table S1. R_i and *C* are from Huang et al., (2012); and are presented in Table S2.

The crop and province dependent burning ratios calculated from the VIIRS-IM/Him data are shown in Fig. 10, alongside the burning ratios from Gao *et al*. (2002). Fig. 10 indicates that there is considerable variation in burning ratios between individual provinces, and that VIIRS-IM/Him wheat burning ratios for are clearly much higher than rice/corn burning ratios. When averaged over the entire Eastern China study area, yearly mean burning ratios from our results for wheat are highest (7.8 - 12%), followed by corn (1.7 - 2.3%), then rice (0.9 - 2.0%). Equivalent mean burning ratios calculated using data from Gao *et al*. (2002) are 9.8 %, 5.9 % and 8.5 %, respectively. While VIIRS-IM/Him wheat residue burning ratios are in reasonable agreement with those used in the various CYBA studies, our rice and corn burning ratios are much lower; this appears to explain why total annual emissions from the VIIRS-IM/Him approach are much lower than the total emissions obtained from the CYBA studies.

Fig. 10 also indicates that burning ratios are not only influenced by crop type and province, but also vary considerably from year to year. For example, in 2012, satellite derived wheat burning ratios for the important agricultural provinces of Anhui (30%), Shandong (11%), Jiangsu (24%) and Henan (11%) are not dissimilar to corresponding ratios (20%, 8%, 10%, 7% respectively) from Gao *et al.,* (2002). However, during 2015, values derived in this study are much lower (Anhui = 6 %; Shandong = 4 %; Jiangsu = 4 %; Henan = 6 %). This interannual variation may be linked with changing local farming activity and prohibition policies (Chen *et al.,* 2017, Li *et al.,* 2016, Yang *et al.,* 2008).

We believe that the disagreement between the burning ratios derived here and those used in CYBA derived studies indicate that emissions inventories derived using traditional CYBAs may be overestimating agricultural burning emissions, for two main reasons: (1) there appears to be considerable uncertainty and subjectivity associated with the methods used to estimating burning ratios used in CYBA studies, and (2) many burning ratios used in CYBA studies are taken from relatively old (>5-10 years) sources of data. For example, Street *et al.* (2003) use data from 1970's, while most ~~later~~ recent researchers use burning ratios from Wang and Zhang (2008) and Gao *et al*. (2002) as listed above in this section.

As shown by this analysis, burning ratios appear to be subject to high spatial and interannual variability due to rapidly changing agricultural policies and decision making that influences the fate of crop residues. As such, in order to ensure reliable emissions estimates, we suggest that future agricultural emission studies and inventories that are based upon CYBAs should endeavour to use burning ratios derived from data (1) with high granularity, and (2) that was collected in the corresponding inventory year.

5.4 Influence of Social Factors on Agricultural Burning

As highlighted in Section 5.2, some studies assume a positive relationship between burning ratio and the mean local income of farmers (Cao *et al.,* 2006; Qin and Xie, 2011). The explanation for this is that higher income areas have better access to electricity and other energy sources, and thus have less need to utilise crop residues for heating and cooking – leading to higher ratios of open burning at these locations. However, this is not what we observe in from analyses carried out for this study. In Fig. 11a, minimal correlation was found between GDP and burning ratio, and there is some suggestion of an inverse relationship between these variables (y=-89x+9542, r^2=0.13). When directly comparing GDP with DMB, as Fig. 12 demonstrates, the provinces with the highest average annual DMB per m^2 (Anhui and Henan; 46 and 27 $g.m^{-2}.yr^{-1}$ respectively) have lower GDP values (US$ 5,580 and 5,335 per capita) than provinces with lower annual DMB densities (e.g. Shandong and Jiangsu, with 15 and 21 $g.m^{-2}.yr^{-1}$ respectively) but high GDP per capita (USD$ 9,882 and 13,311 respectively). In fact, across the eastern China study area, our annual total DMB metric was found to be somewhat inversely correlated with GDP per capita (r^2 = 0.33; Fig. 11b).

We theorise that the observed inverse correlation between GDP and DMB results from the fact that alternative residue disposal methods to biomass burning have a relatively high cost, and can only be afforded by wealthier farmers/provinces. For example, the local government of Jiangsu Province (a relatively wealthy province [$ 13,311 per capita] with only moderate DMB [21 $g.m^{-2}.yr^{-1}$]) released a regulation in 2009 stating that by the end of 2012, over 35% of crop residues should been incorporated into the soil after mechanised harvesting. The regulation also indicated that the local government should include a budget for improving the efficiency of agricultural machinery and subsidise farmers who follow this regulation. Furthermore, alternative uses for crop residues are often expensive, and are likely only a viable option in relatively wealthy areas. For example, research on residue burning for power generation shows the government needs to pay at least 20% of the total cost of the operation to keep the power plants running, partly because of the high costs associated with residue collection and transportation from the fields (Li and Hu, 2009).

In addition to influencing the quantity of material burned and when it is burned, societal factors also appear influence the spatial pattern of burning within provinces, and at more granular levels such as at the 0.1^{o} grid cell level. The work presented in Section 5.1 suggests that the winter burning season (Nov-Dec) is caused by delayed burning of residues left over from the autumn harvest season, because of prohibition policies related to burning being more robustly enforced earlier in the season. Fig. 6 also showed that the spatial distribution of FRE areal density during winter is different from the normal autumn burning season that occurs in Sep-Oct. Generally, the areas of strongest burning are further from the provincial capital cities (marked by the green stars in Fig. 6) during autumn. For example, fires in Anhui Province are mainly distributed in the north during autumn, whilst fire locations change to the south (closer to the capital city of Hefei) during the delayed winter burns. A similar example can also be seen in Hubei Province, where fires shift from west to east from the autumn to winter burning seasons.

To examine this in a more quantitative manner, we calculated the distance from each grid cell shown in Fig. 6 to their provincial capitals. Fig. 13 shows the normalised frequency distribution of the distance from the capital to the top 10% of FRE releasing grid cells in each province, using data from the four burning seasons during the 2012-2015 period. The first and third distance quartiles during the autumn season are 109 km and 214 km respectively, but for the 'lagged' winter burning season, the distribution shifts to far shorter distances (first and third quartiles of 70 km and 153 km respectively). Similarly, the mean distance from provincial capitals also decreased from 165 km in autumn to 124 km in winter. A Kolmogorov–Smirnov (K-S) test was performed to evaluate the difference between the distributions of distance data for the autumn and winter burning seasons, and the resulting high K-S statistic (0.30, $p < 0.001$) indicates that the distribution of distances during the winter months is substantially different to the autumn distance distribution. Similar results were found when we applied the K-S test to each calendar year of data separately (not shown). One possible explanation for this observed difference is that the geographical shift might also be linked with the policies aimed at prohibiting burning, since areas close to capital cities are likely to have more resources for enforcing the prohibition compared to areas more distant from the major urban populations.

6. SUMMARY AND CONCLUSION

We have developed a new state-of-the-art agricultural burning emissions inventory ('VIIRS-IM/Him') for eastern China by combining fire radiative power (FRP) observations from the VIIRS and Himawari-8 sensors for the 2012-2015 period. While several other studies have also used satellite EO data to develop such inventories, they have all relied on MODIS fire products for their source observations. Such inventories include the global GFED and GFAS inventories, several Chinese regional studies (e.g. Huang et al., 2012, Liu et al., 2015). MODIS fire products are known to show very high omission rates in environments dominated by small agricultural fires (Randerson et al., 2012; Zhang et al., 2017, 2018), but the 'small fire optimised' VIIRS-IM product of Zhang et al. (2017) used in this study detects far more of the fire activity across eastern China and on average show FRP totals around 4x higher than those of the MODIS AF products. To convert the twice-daily VIIRS-IM FRP product information to daily time-integrated FRE, we have used new diurnal fire cycle data from Himawari-8, a geostationary satellite positioned over east Asia that can best capture the specific diurnal fire variability of the agricultural burning regions.

Our final VIIRS/Him agricultural fire emissions inventory reports dry matter burned (DMB) totals around 2-5× higher than is reported by GFAS and GFED 4.1s in eastern China for corresponding time periods. Use of a crop rotation map allowed our VIIRS-IM/Him fire and emissions outputs to be disaggregated by individual crop types, and we found wheat residue burning to be the primary agricultural emission source, accounting for over 50% of the total emissions each year for all investigated smoke constituents (CO_2, CO, $PM_{2.5}$ and black carbon). A strong seasonal variation in fire activity and emissions is seen, with annual peak activity occurring in summer (May-June) as a result of wheat residue burning, and a smaller secondary activity peak occurring in autumn (Sept-Oct) as a result of corn and rice residue burning. Furthermore, we discovered a new winter (Nov-Dec) agricultural residue burning season. As no crop harvesting occurs during winter, we suspect that this fire activity results from farmers burning previously stored residues from the autumn harvest in winter, after autumn residue burning prohibitions have been lifted. This theory is supported by our observation of statistically distinct spatial burning patterns in the autumn and winter seasons; the majority of autumn burning occurs at a greater distance from provincial capitals than the winter burning does. This may reflect stronger enforcement of autumn residue burning prohibition measures in close proximity to major urban population centres than in rural locations. Farmers in areas with stronger prohibition enforcement (typically closer to urban areas) then burn their agricultural residue in winter.

Detailed comparison to existing inventories showed that our VIIRS-IM/Him annual emissions totals are 1.2-4.7× greater than those reported by GFAS, and 0.5-1.7x those reported by GFED4.1s, with some inter-species variability due to the use of different emissions factors between the inventories. By contrast, the VIIRS-IM/Him inventory shows emissions totals that are on average lower than those from emission inventories derived using crop yield based approaches (CYBA) by a factor of 2-5x. This discrepancy is believed to be primarily due to many CYBAs using outdated and/or inappropriate burning ratios, that consequently leads to CYBAs overestimating the amount of crop residue DMB annually. Back calculated burning ratios from the VIIRS-IM/Him data suggest that burning ratios for rice and corn are much lower than the CYBA literature suggests (approx. 0.9-2.3 % rather than 11-33 %). We also noted considerable inter-provincial and interannual variation in these back calculated burning ratios, for example, wheat burning ratios significantly decrease over our four-year study period. This strongly suggests that high spatial resolution, up-to-date burning ratios should always be used in CYBA for agricultural burning fire emission estimation. Furthermore, several CYBA approaches (e.g. Sun *et al.,* 2016, Zhao *et al.,* 2015) have derived burning ratios from provincial GDP data, assuming a positive relationship between these variables (Cao *et al.*, 2006). However, we found evidence of an opposite (i.e. negative) relationship between provincial GDP and the amount of DMB in agricultural fires, hypothesised to be due to the higher cost of disposal of crop residues by non-biomass burning methods. This suggests that great care needs to be taken when deriving burning ratios for use in future agricultural emissions inventories based upon CYBA methods, and that satellite remote sensing approaches based on EO datasets that adequately detect the presence of agricultural fires are a far better approach to fire emissions estimation in such environments.

ACKNOWLEDGEMENTS

This work has been supported by the NERC National Centre for Earth Observation (NE/R000115/1) and specifically by NERC Grant NE/M017729/1. The VIIRS SDR and MODIS data were retrieved from CLASS and Reverb, and are courtesy of the NASA EOSDIS LP DAAC and USGS EROS Centre, South Dakota. GFAS data was generated using Copernicus Atmosphere Monitoring Service Information, operated by ECMWF. All data storage and processing were conducted using the UK's JASMIN super-data-cluster system, managed by UK STFC's Centre for Environmental Data Analysis (CEDA).

REFERENCES

Andela, N., Kaiser, J.W., Van der Werf, G.R. and Wooster, M.J., 2015. New fire diurnal cycle characterizations to improve fire radiative energy assessments made from MODIS observations. Atmospheric Chemistry and Physics, 15(15), pp.8831-8846.

Andreae, M. O. & Merlet, P. 2001. Emission of trace gases and aerosols from biomass burning. Global biogeochemical cycles, 15(4), pp 955-966.

Bond, T. C., Doherty, S. J., Fahey, D., Forster, P., Berntsen, T., DeAngelo, B., Flanner, M., Ghan, S., Kärcher, B. & Koch, D. 2013. Bounding the role of black carbon in the climate system: A scientific assessment. Journal of Geophysical Research: Atmospheres, 118(11), pp 5380-5552.

Cao, G., Zhang, X. & Zheng, F. 2006. Inventory of black carbon and organic carbon emissions from China. Atmospheric Environment, 40(34), pp 6516-6527.

Chan, C. K. & Yao, X. 2008. Air pollution in mega cities in China. Atmospheric Environment, 42(1), pp 1-42.

Cheng, Y., Engling, G., He, K. B., Duan, F. K., Ma, Y. L., Du, Z. Y., Liu, J. M., Zheng, M. & Weber, R. J. 2013. Biomass burning contribution to Beijing aerosol. Atmos. Chem. Phys., 13(15), pp 7765-7781.

Chen, J., Chen, J., Liao, A., Cao, X., Chen, L., Chen, X., He, C., Han, G., Peng, S., Lu, M., Zhang, W., Tong, X., Mills, J., 2015. Global land cover mapping at 30m resolution: A POK-based operational approach. ISPRS J. Photogramm. Remote Sens., Global Land Cover Mapping and Monitoring 103, 7–27. https://doi.org/10.1016/j.isprsjprs.2014.09.002

Chen, J., Li, C., Ristovski, Z., Milic, A., Gu, Y., Islam, M.S., Wang, S., Hao, J., Zhang, H., He, C. and Guo, H., 2017. A review of biomass burning: Emissions and impacts on air quality, health and climate in China. Science of the Total Environment.

Du, H., Kong, L., Cheng, T., Chen, J., Du, J., Li, L., Xia, X., Leng, C. & Huang, G. 2011. Insights into summertime haze pollution events over Shanghai based on online water-soluble ionic composition of aerosols. Atmospheric Environment, 45(29), pp 5131-5137.

Ellicott, E., Vermote, E., Giglio, L. and Roberts, G., 2009. Estimating biomass consumed from fire using MODIS FRE. Geophysical Research Letters, 36(13).

Freeborn, P. H., Wooster, M. J., Hao, W. M., Ryan, C. A., Nordgren, B. L., Baker, S. P. & Ichoku, C. 2008. Relationships between energy release, fuel mass loss, and trace gas and aerosol emissions during laboratory biomass fires. Journal of Geophysical Research: Atmospheres, 113(D1), pp D01301.

Fu, J. Y., Jiang, D., Huang, Y. H., 2014a. 1-km grid population dataset of China, Global Change Research Data Publishing & Repository, DOI:10.3974/geodb.2014.01.06.V1

Fu, J. Y., Jiang, D., Huang, Y. H., 2014b. 1-km grid GDP dataset of China, Global Change Research Data Publishing & Repository, DOI:10.3974/geodb.2014.01.07.V1Gao, X., Ma, W., Ma, C., Zhang, F., Wang, Y., 2002. Analysis of the current status of utilization of crop straw in China. Journal of Huazhong Agricultural University 21, 242–247 (in Chinese).

Giglio, L., Csiszar, I. & Justice, C. 2006. Global distribution and seasonality of active fires as observed with the Terra and Aqua Moderate Resolution Imaging Spectroradiometer (MODIS) sensors. J. Geophys. Res, 111(G02016.

Giglio, L., Randerson, J.T. and Werf, G.R., 2013. Analysis of daily, monthly, and annual burned area using the fourth-generation global fire emissions database (GFED4). Journal of Geophysical Research: Biogeosciences, 118(1), pp.317-328.

Goldberg, M.D., Kilcoyne, H., Cikanek, H., Mehta, A., 2013. Joint Polar Satellite System: The United States next generation civilian polar-orbiting environmental satellite system. J. Geophys. Res. Atmospheres 118, 13,463-13,475. https://doi.org/10.1002/2013JD020389

He, M., Zheng, J., Yin, S. & Zhang, Y. 2011. Trends, temporal and spatial characteristics, and uncertainties in biomass burning emissions in the Pearl River Delta, China. Atmospheric Environment, 45(24), pp 4051-4059.

Huang, X., Li, M., Li, J. & Song, Y. 2012. A high-resolution emission inventory of crop burning in fields in China based on MODIS Thermal Anomalies/Fire products. Atmospheric Environment, 50(0), pp 9-15.

Jiang, D., Zhuang, D., Fu, J., Huang, Y. & Wen, K. 2012. Bioenergy potential from crop residues in China: Availability and distribution. Renewable and Sustainable Energy Reviews, 16(3), pp 1377-1382.

Kaiser, J. W., Heil, A., Andreae, M. O., Benedetti, A., Chubarova, N., Jones, L., Morcrette, J. J., Razinger, M., Schultz, M. G., Suttie, M. & van der Werf, G. R. 2012. Biomass burning emissions estimated with a global fire assimilation system based on observed fire radiative power. Biogeosciences, 9(1), pp 527-554.

Li, W., Shao, L. & Buseck, P. 2010. Haze types in Beijing and the influence of agricultural biomass burning. Atmospheric Chemistry and Physics, 10(17), pp 8119-8130.

Li, J.F. and Hu, Y.S., 2009. Analysis on investment and operation of straw-fired power plants in Jiangsu province. Electric power technologic economics, 5, p.005 (in Chinese).

Li, J., Li, Y., Bo, Y. and Xie, S., 2016. High-resolution historical emission inventories of crop residue burning in fields in China for the period 1990–2013. Atmospheric Environment, 138, pp.152-161.

~~Li, M., Q. Zhang, D. Streets, K. B. He, Y. F. Cheng, L. K. Emmons, H. Huo, S. C. Kang, Z. Lu, M. Shao, H. Su, X. Yu, and Y. Zhang (2014), Mapping Asian anthropogenic emissions of non-methane volatile organic compounds to multiple chemical mechanisms, Atmos. Chem. Phys., 14, 5617-5638.~~

Li, M., Zhang, Q., Kurokawa, J.I., Woo, J.H., He, K.B., Lu, Z., Ohara, T., Song, Y., Streets, D.G., Carmichael, G.R. and Cheng, Y.F., 2015. MIX: a mosaic Asian anthropogenic emission inventory for the MICS-Asia and the HTAP projects. Atmos. Chem. Phys. Discuss, 15(23), pp.34813-34869.

Liu, M., Song, Y., Yao, H., Kang, Y., Li, M., Huang, X. and Hu, M., 2015. Estimating emissions from agricultural fires in the North China Plain based on MODIS fire radiative power. Atmospheric environment, 112, pp.326-334.

Liu, H., Jiang, G. M., Zhuang, H. Y. & Wang, K. J. 2008. Distribution, utilization structure and potential of biomass resources in rural China: With special references of crop residues. Renewable and Sustainable Energy Reviews, 12(5), pp 1402-1418.

NBSC (National Bureau of Statistic of China) China Statistical Yearbook, 480 2003–2015, China Statistics Press, Beijing (2004–2016) (in Chinese).

Portmann, F. T., Siebert, S. & Döll, P. 2010. MIRCA2000—Global monthly irrigated and rainfed crop areas around the year 2000: A new high-resolution data set for agricultural and hydrological modeling. Global Biogeochemical Cycles, 24(1).

Qin, Y. & Xie, S. D. 2011. Historical estimation of carbonaceous aerosol emissions from biomass open burning in China for the period 1990–2005. Environmental Pollution, 159(12), pp 3316-3323.

Randerson, J., Chen, Y., Werf, G., Rogers, B. & Morton, D. 2012. Global burned area and biomass burning emissions from small fires. Journal of Geophysical Research: Biogeosciences (2005–2012), 117(G4), pp.

Roberts, G., Wooster, M.J. and Lagoudakis, E., 2009. Annual and diurnal african biomass burning temporal dynamics. Biogeosciences, 6(5), pp.849-866.

Roberts, G., Wooster, M.J., Xu, W., Freeborn, P.H., Morcrette, J.J., Jones, L., Benedetti, A. and Kaiser, J., 2015. LSA SAF Meteosat FRP Products: Part 2--Evaluation and demonstration of use in the Copernicus Atmosphere Monitoring Service (CAMS). Atmospheric Chemistry & Physics Discussions, 15(12).

Schroeder, W., Oliva, P., Giglio, L. and Csiszar, I.A., 2014. The New VIIRS 375 m active fire detection data product: Algorithm description and initial assessment. Remote Sensing of Environment, 143, pp.85-96.

Streets, D.G., Yarber, K.F., Woo, J.H. and Carmichael, G.R., 2003. Biomass burning in Asia: Annual and seasonal estimates and atmospheric emissions. Global Biogeochemical Cycles, 17(4).

Sun, J., Peng, H., Chen, J., Wang, X., Wei, M., Li, W., Yang, L., Zhang, Q., Wang, W. & Mellouki, A. 2016. An estimation of CO2 emission via agricultural crop residue open field burning in China from 1996 to 2013. Journal of Cleaner Production, 112, Part 4(2625-2631.

van der Werf, G. R., Randerson, J. T., Giglio, L., Collatz, G. J., Mu, M., Kasibhatla, P. S., Morton, D. C., DeFries, R. S., Jin, Y. & van Leeuwen, T. T. 2010. Global fire emissions and the contribution of deforestation, savanna, forest, agricultural, and peat fires (1997–2009). Atmos. Chem. Phys., 10(23), pp 11707-11735.

van der Werf, G. R., Randerson, J. T., Giglio, L., van Leeuwen, T. T., Chen, Y., Rogers, B. M., Mu, M., van Marle, M. J. E., Morton, D. C., Collatz, G. J., Yokelson, R. J., and Kasibhatla, P. S.: Global fire emissions estimates during 1997–2016, Earth Syst. Sci. Data, 9, 697-720, https://doi.org/10.5194/essd-9-697-2017, 2017.

Wang & Zhang, 2016, http://news.chengdu.cn/2016/1106/1829718.shtml,Chengdu Business Daily

Wang, S. & Zhang, C. 2008. Spatial and temporal distribution of air pollutant emissions from open burning of crop residues in China. Sciencepaper online, 3(5), pp 329-333.

Wolfe, R.E., Lin, G., Nishihama, M., Tewari, K.P., Tilton, J.C. and Isaacman, A.R., 2013. Suomi NPP VIIRS prelaunch and on-orbit geometric calibration and characterization. Journal of Geophysical Research: Atmospheres, 118(20), pp.11-508.

Wooster, M. J., Roberts, G., Perry, G. L. W. & Kaufman, Y. J. 2005. Retrieval of biomass combustion rates and totals from fire radiative power observations: FRP derivation and calibration relationships between biomass consumption and fire radiative energy release. Journal of Geophysical Research: Atmospheres, 110(D24), pp D24311.

Xu, W., Wooster, M.J., Kaneko, T., He, J., Zhang, T. and Fisher, D., 2017. Major advances in geostationary fire radiative power (FRP) retrieval over Asia and Australia stemming from use of Himarawi-8 AHI. Remote Sensing of Environment, 193, pp.138-149.

Yamaji, K., Li, J., Uno, I., Kanaya, Y., Irie, H., Takigawa, M., Komazaki, Y., Pochanart, P., Liu, Y., Tanimoto, H., Ohara, T., Yan, X., Wang, Z. & Akimoto, H. 2010. Impact of open crop residual burning on air quality over Central Eastern China during the Mount Tai Experiment 2006 (MTX2006). Atmos. Chem. Phys., 10(15), pp 7353-7368.

Yan, X., Ohara, T. & Akimoto, H. 2006. Bottom-up estimate of biomass burning in mainland China. Atmospheric Environment, 40(27), pp 5262-5273.

Yang, S., He, H., Lu, S., Chen, D. & Zhu, J. 2008. Quantification of crop residue burning in the field and its influence on ambient air quality in Suqian, China. Atmospheric Environment, 42(9), pp 1961-1969.

Za, 2015, http://www.chinanews.com/sh/2015/11-04/7606112.shtml, Legislative Evening Newspaper

Zhang, H., Ye, X., Cheng, T., Chen, J., Yang, X., Wang, L. & Zhang, R. 2008. A laboratory study of agricultural crop residue combustion in China: Emission factors and emission inventory. Atmospheric Environment, 42(36), pp 8432-8441.

Zhang, L., Liu, Y. and Hao, L., 2016. Contributions of open crop straw burning emissions to PM2. 5 concentrations in China. Environmental Research Letters, 11(1), p.014014.

Zhang, T., Wooster, M.J., Green, D.C. and Main, B., 2015. New field-based agricultural biomass burning trace gas, PM2. 5, and black carbon emission ratios and factors measured in situ at crop residue fires in Eastern China. Atmospheric Environment, 121, pp.22-34.

Zhang, T., Wooster, M.J. and Xu, W., 2017. Approaches for synergistically exploiting VIIRS I-and M-Band data in regional active fire detection and FRP assessment: A demonstration with respect to agricultural residue burning in Eastern China. Remote sensing of environment, 198, pp.407-424.

Zhang, T., Wooster, M., de Jong, M. and Xu, W., 2018. How Well Does the 'Small Fire Boost'Methodology Used within the GFED4. 1s Fire Emissions Database Represent the Timing, Location and Magnitude of Agricultural Burning?. Remote Sensing, 10(6), p.823.

Zhao, H., Tong, D. Q., Gao, C. & Wang, G. 2015. Effect of dramatic land use change on gaseous pollutant emissions from biomass burning in North Eastern China. Atmospheric Research, 153(429-436).

Zhou, L., Divakarla, M., Liu, X., Layns, A., Goldberg, M., 2019. An Overview of the Science Performances and Calibration/Validation of Joint Polar Satellite System Operational Products. Remote Sens. 11, 698. https://doi.org/10.3390/rs11060698

Zuo 2015, http://www.chinanews.com/gn/2015/12-11/7666514.shtml, Anhui News

Table 1: Emission Factors for agricultural residue burning used in this study. Wheat and rice emission factors were derived from field measurements conducted in eastern China and reported by Zhang et al. (2015), while the corn emission factors are from Andreae and Merlet (2001), the same as those used in GFAS (Kaiser *et al.*, 2012). *$PM_{2.5}$ = particulate matter with diameter < 2.5μm

	Emissions Factor ($g.kg^{-1}$)		
	Wheat	Corn	Rice
CO_2	1739±19	1308±14	1761±30
CO	60±12	92±18	47±19
$PM_{2.5}$*	6.1±1.3	8.3±1.8	9.6±4.3
Black Carbon	0.70±0.09	0.42±0.05	0.56±0.04

Table 2: Total species-specific fire emissions calculated in this study for agricultural burning in eastern China, and comparison to those contained within other fire emissions inventories and calculated in previous studies.

Reference	Region	Year	Method	Emissions ($Gg.yr^{-1}$)			
				CO_2	CO	$PM_{2.5}$	BC
This study	Eastern China	2012	Satellite	31066 ± 1960	1035±327	124±43	11±1.8
		2013		31107 ± 1748	1025±320	130±44	11±1.7
		2014		27069 ± 1421	904±279	107±36	10±1.5
		2015		16932 ± 1044	562±177	70±24	6±0.95
GFAS	Eastern China	2012	Satellite	9219	649	58	3.0
Kaiser *et al.,* 2012		2013		8173	576	52	2.6
		2014		8760	617	55	2.8
		2015		6818	480	43	2.2
GFED4.1s	Eastern China	2012	Satellite	18629	1199	74	8.8
Van der Werf *et al*., 2017		2013		24034	1547	95	11
		2014		18241	1173	72	8.6
		2015		15892	1023	63	7.5
Liu *et al.,* 2015	NCP[1]	2012	Satellite	26000	1700	102	13
		2013		9800	630	39	5
		2014		13000	820	50	6
Zhang et al., 2008	Eastern China[3]	2004	CYBA[2]	67703	5624	-	-
Huang et al., 2012	Eastern China[3]	2006	CYBA	41374	2668	164	20
Qiu et al., 2016	Eastern China	2013	CYBA	72071	2549	445	42
Li et al., 2016	NCP	2012	CYBA	68675	5983	452	23
Sun et al., 2016	China	2013	CYBA	192540	-	-	-
Street *et al*., 2003	China	2000	CYBA	160000	10000	-	70
Yan *et al*., 2006	China	2000	CYBA	184000	11000	470	80

[1] NCP refers to the North China Plain, which has a geographic extent similar to that of this study (32-41ºN, 113-121ºE).
[2] CYBA refers to Crop Yield Based Approaches, see Section 2.6.1
[3] Sum of provinces/cities shown in Fig.1 of this study.

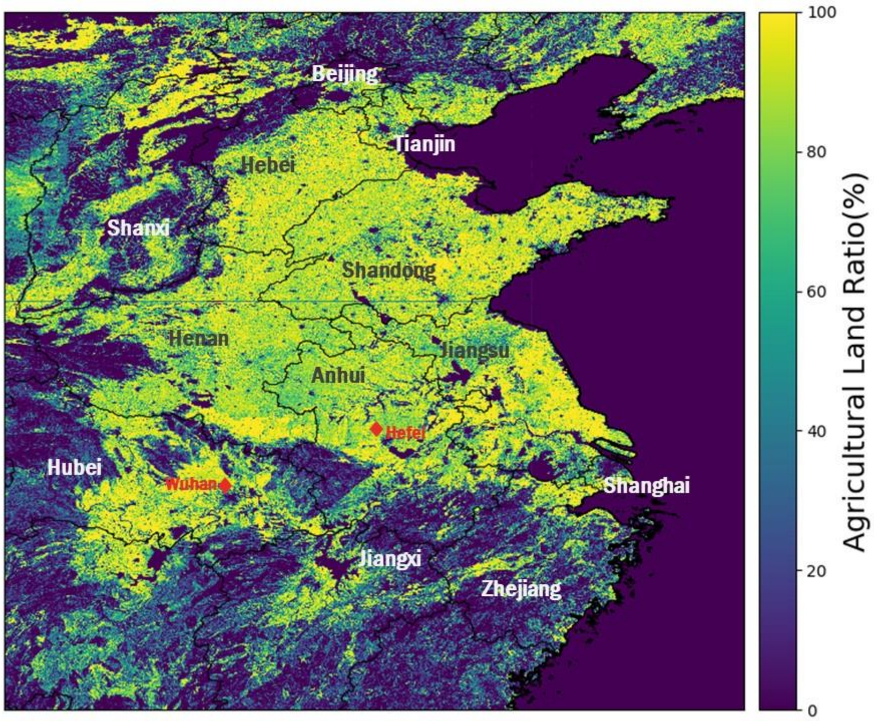

Figure 1: The spatial extent of the study area (111-123° E, 27-40° N). The agricultural land ratio taken from the GlobeLand30 land cover product (Chen et al, 2015) was re-gridded to 0.01 degree spatial resolution, and is overlain with the main provinces, mega-cities and some important provincial capital cities in eastern China. The basic layer of country/province borders within this map was created using Python Basemap librabry.

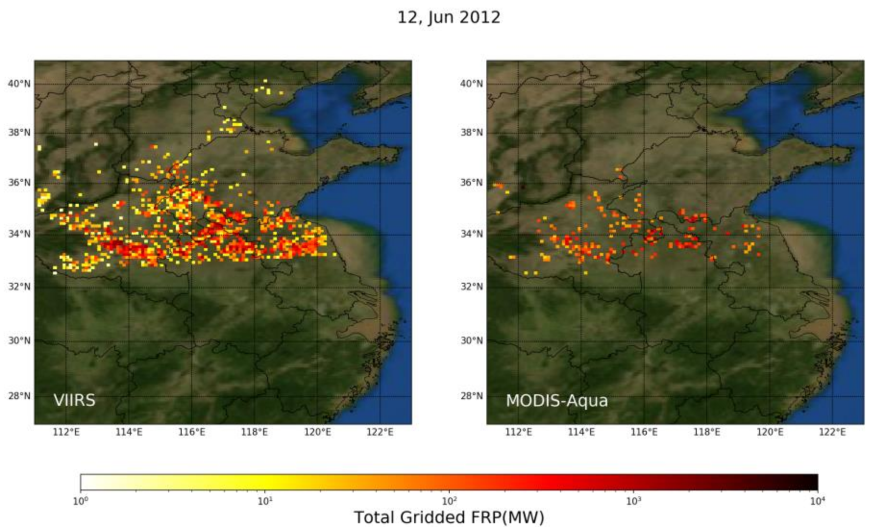

Figure 2: Example of the spatial distribution of total gridded FRP (MW; calculated per 0.1° grid cell) calculated from near simultaneous VIIRS-IM and MODIS Aqua data collected over the eastern China study area of Fig. 1 on June 12th, 2012. The VIIRS-IM data product clearly quantifies a higher proportion of the FRP from fires burning in the region at the time of the satellite overpass than MODIS Aqua does. The basic layer of country/province borders within this map was created using Python Basemap librabry.

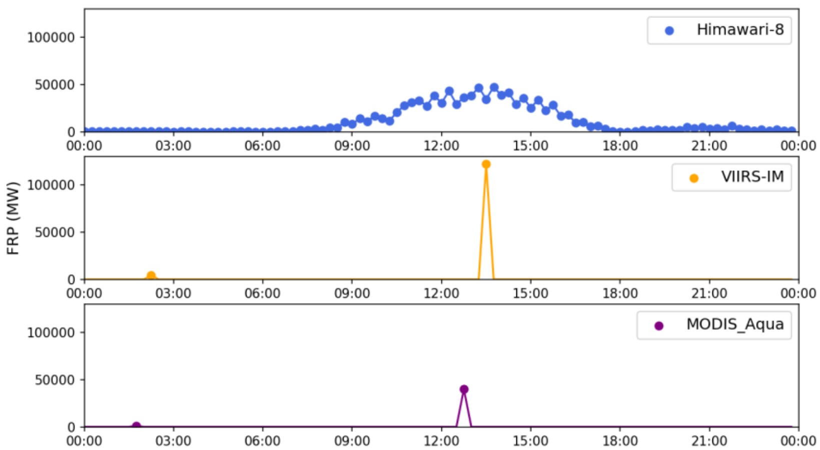

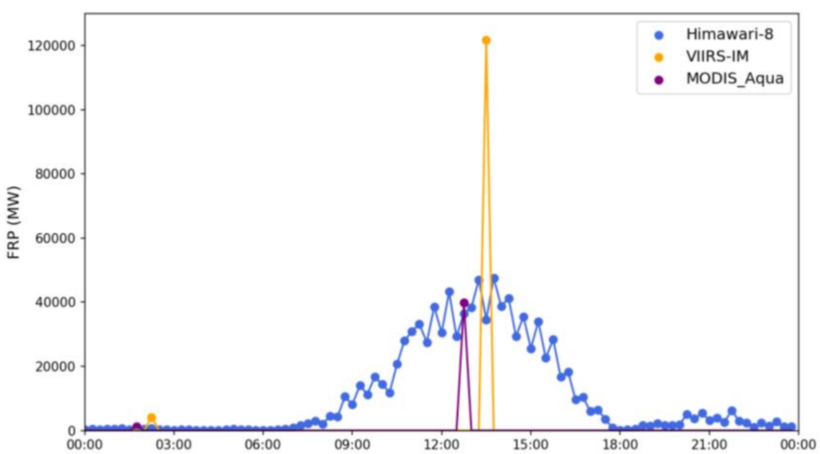

Figure 3: Time series of spatially summed FRP for eastern China, as retrieved from geostationary Himawari, and polar-orbiting VIIRS-IM and MODIS observations made on June 11th, 2015. VIIRS and MODIS Aqua provide typically two observations per day, and sometimes three when the swath overlaps from different orbits occur. Himawari provides 144 observations per day.

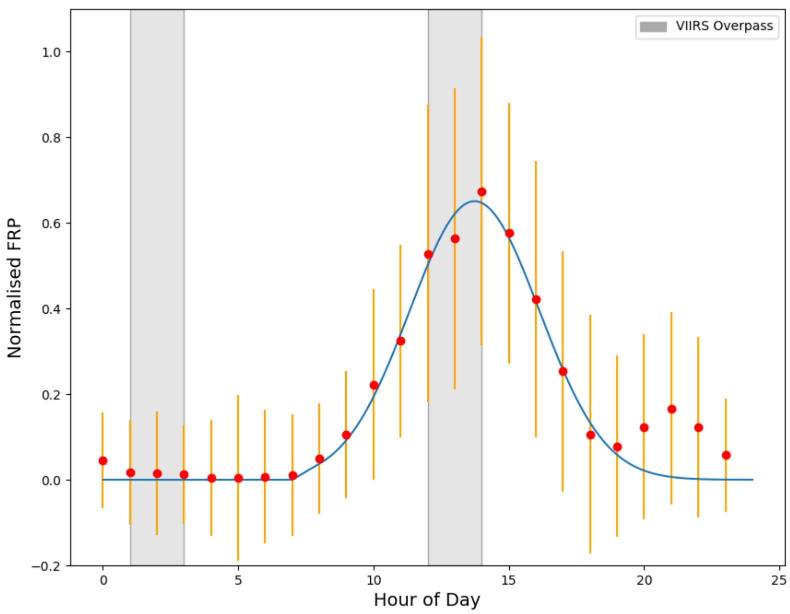

Figure 4: Time series of hourly normalised fire radiative power derived from Himawari-8 FRP data generated using the algorithm of Xu et al. (2017) over eastern China at 0.1 degree for June 2015 (the 'Summer' diurnal fire cycle). The blue curve shows the best fit of the Gaussian distribution, with orange error bar show standard deviation. Grey shading shows the two daily VIIRS overpass periods.

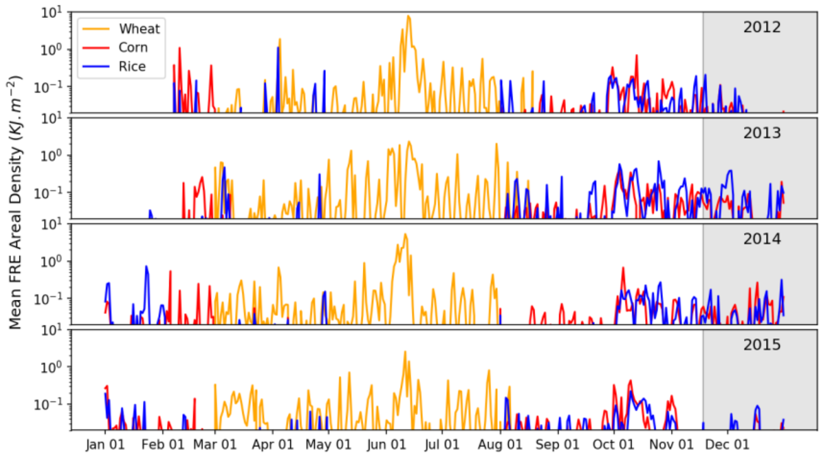

Figure 5: Time-series of mean daily FRE areal density (kJ m^{-2}, calculated per 0.1° grid cell) from 2012-2015 for the entire study area disaggregated by crop residue type (wheat, corn and rice) according to the method described in Section 2.4. Grey shaded areas highlighted the usual newly discovered winter burning season from mid-November to December when no crop harvesting occurs but where fires are clearly occurring. This period of agricultural burning is discussed further in Section 5.1

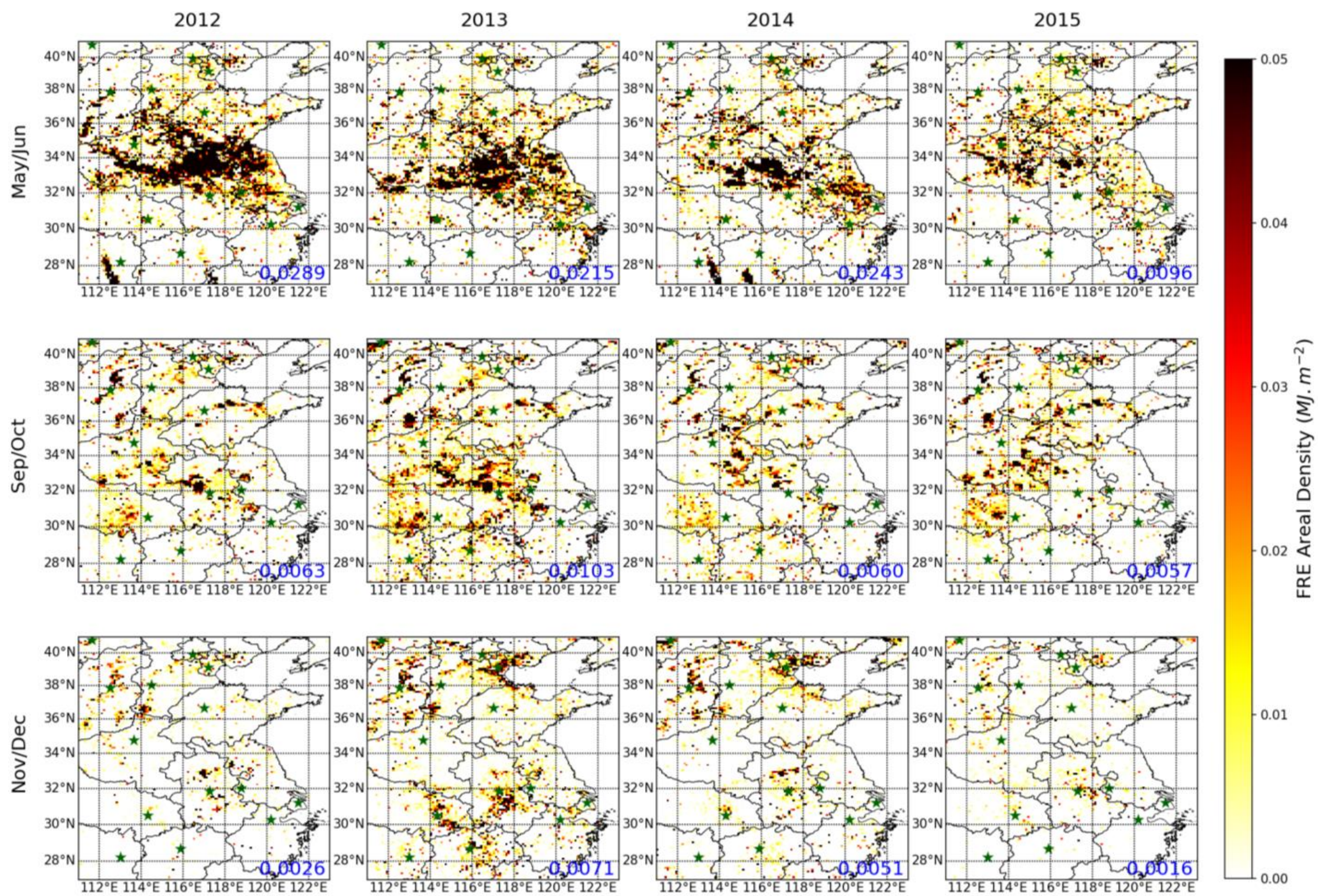
2012
2013
2014
2015
May/Jun
Sep/Oct
Nov/Dec
0.0289
0.0215
0.0243
0.0096
0.0063
0.0103
0.0060
0.0057
0.0026
0.0071
0.0051
0.0016
40°N
38°N
36°N
34°N
32°N
30°N
28°N
112°E 114°E 116°E 118°E 120°E 122°E
FRE Areal Density ($MJ.m^{-2}$)
0.00
0.01
0.02
0.03
0.04
0.05

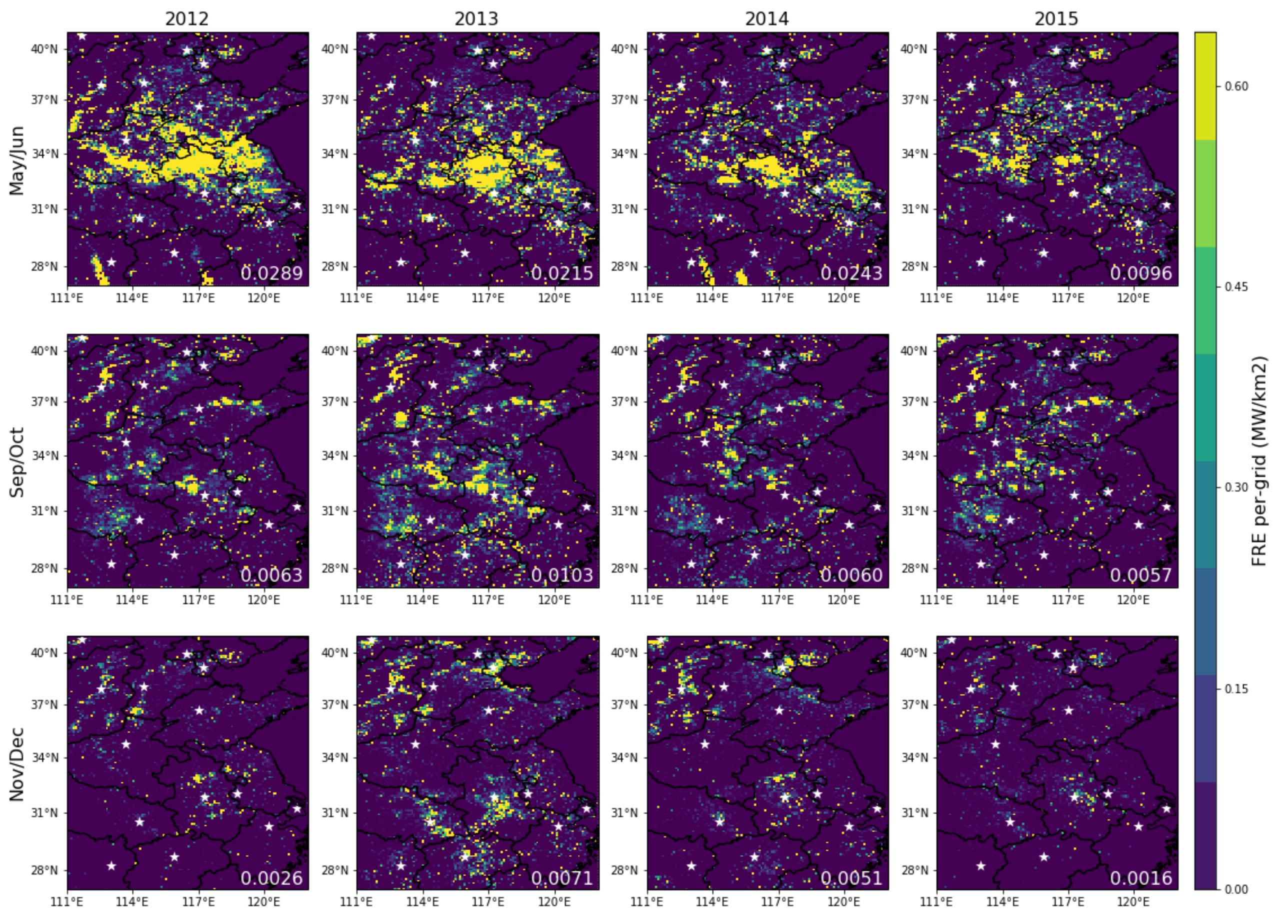

Figure 6: Spatial distribution of FRE areal density (MJ.m^{-2}, 0.1 deg grid cells) for agricultural fires in eastern China from 2012 to 2015 (top to bottom rows) split by fire season: summer (May-June, top row), autumn (Sep-Oct, middle row) and winter (Nov-Dec, bottom row). Mean regional FRE for each season is indicated in ~~blue~~ white text, and the capital city location of each province is shown as a ~~green~~ white star on each map. The basic layer of country/province borders within this map was created using Python ~~Basemap~~ Cartopy librabry.

Formatted: Centered

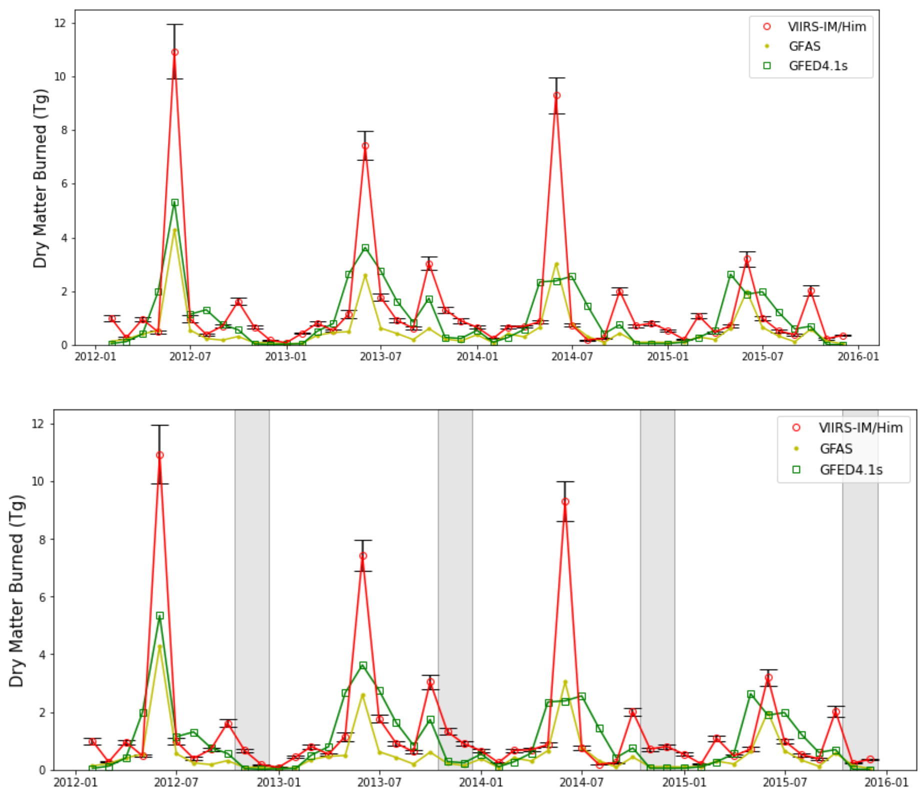

Figure 7: Monthly (2012-2015) time-series of total dry matter burned (DMB) retrieved using the VIIRS-IM/Him FRP product developed in this study (with standard deviation shown as black error bars), along with comparable GFAS and GFED4.1s DMB totals.

Grey shaded areas highlighted the winter burning season from mid-November to December (Section 5.1).

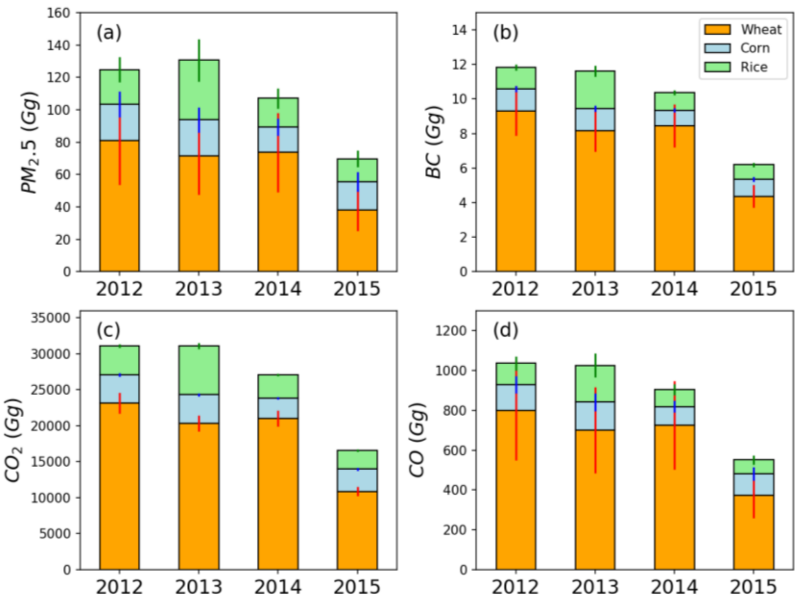

(a)
(b)
(c)
(d)
$PM_2.5$ (Gg)
BC (Gg)
CO_2 (Gg)
CO (Gg)
Wheat
Corn
Rice
2012
2013
2014
2015

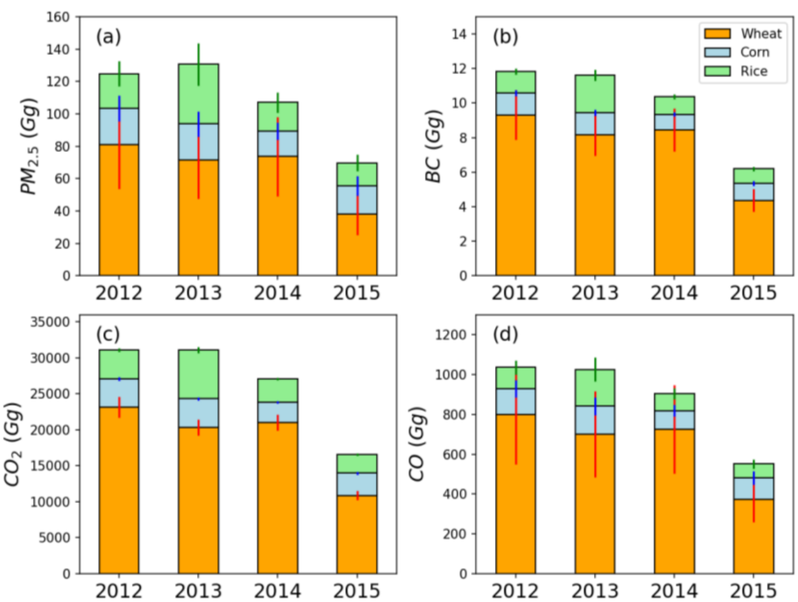

(a)
(b)
(c)
(d)
$PM_{2.5}$ (Gg)
BC (Gg)
CO_2 (Gg)
CO (Gg)
Wheat
Corn
Rice
2012
2013
2014
2015

Figure 8: Annual total $PM_{2.5}$, BC, CO_2, and CO emissions for eastern China for the three main crop residues burning types (wheat, corn, rice) calculated for 2012-2015 using the VIIRS-IM/Him based emissions inventory developed herein. Coloured error bars indicate 1 standard deviation.

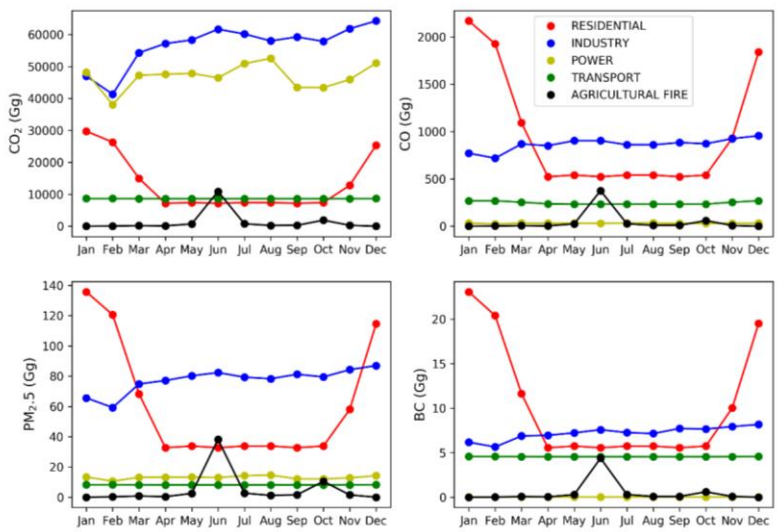

Figure 9: Comparison of monthly CO_2, CO, $PM_{2.5}$ and BC emissions from agricultural fires with those from other emission sources (residential, industry, power, transport, data source: Li et al., 2015) in the intensive burning area (32-36° N, 112-122° E) of eastern China in the year 2013.

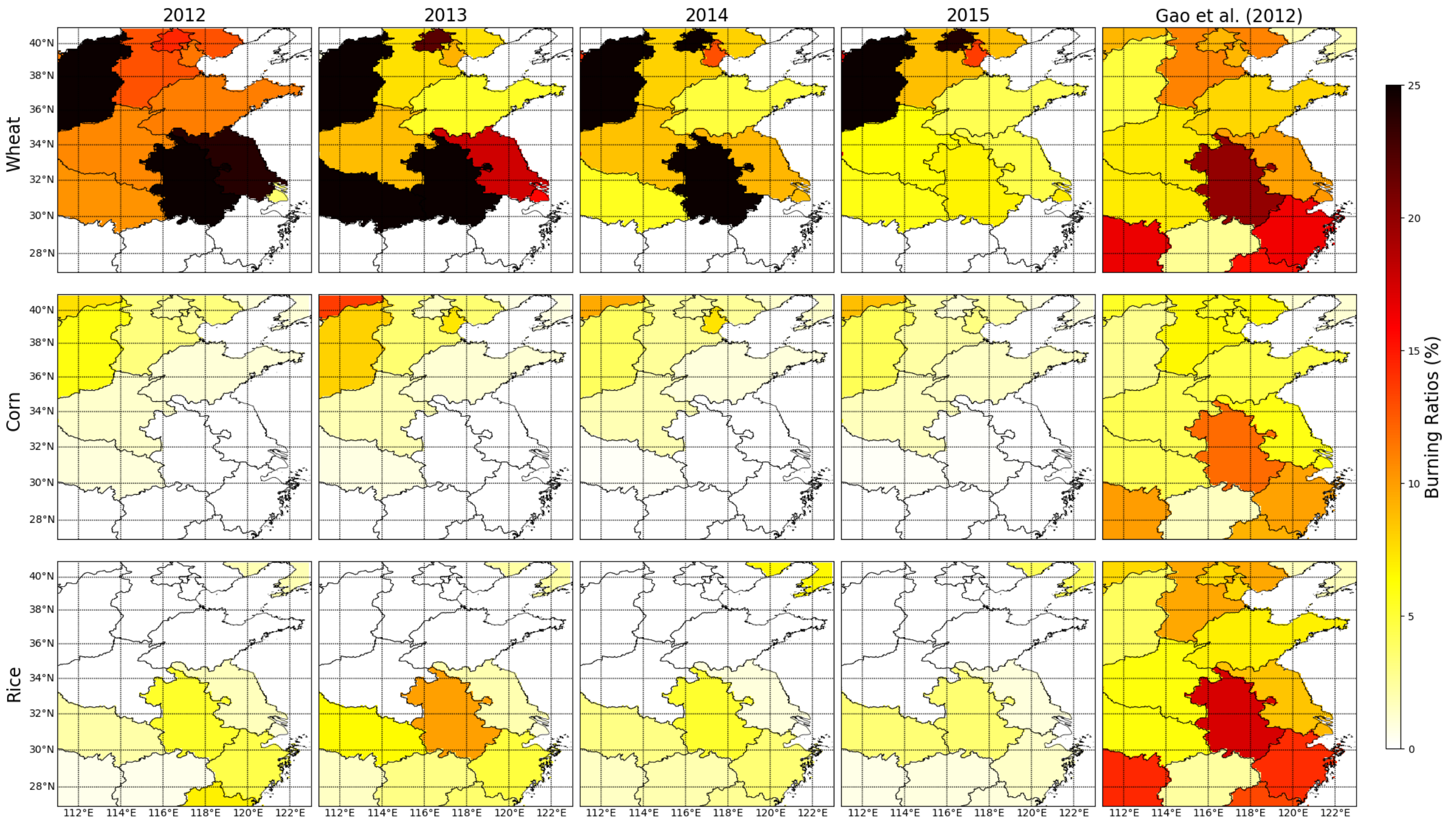

Figure 10: Temporal and spatial- variability of province-specific percentages of crop residues burned in the fields (burning ratio metrics) of eastern China. Data are calculated using crop yield estimates from National Bureau of Statistics of China and the dry matter burned totals derived herein using our VIIRS-IM/Him DMB datasets from 2012-2015, and compared to the temporally invariant estimates provided by Gao et al., (2002, final column). The basic layer of country/province borders within this map was created using Python Basemap librabry.

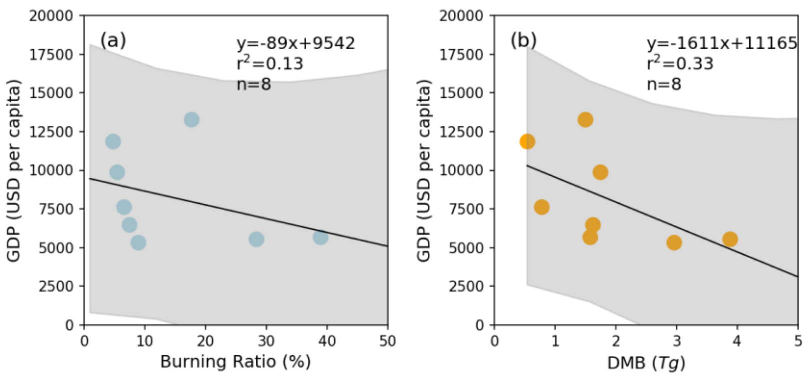

Figure 11: Direct comparisons of mean GDP per capita with (a) burning ratio for wheat from 2012, (b) province-specific yearly dry matter burned (DMB). The best fit linear relationships are shown, along with its equation, and the grey shaded area represents the 95% confidence limit on the relationship.

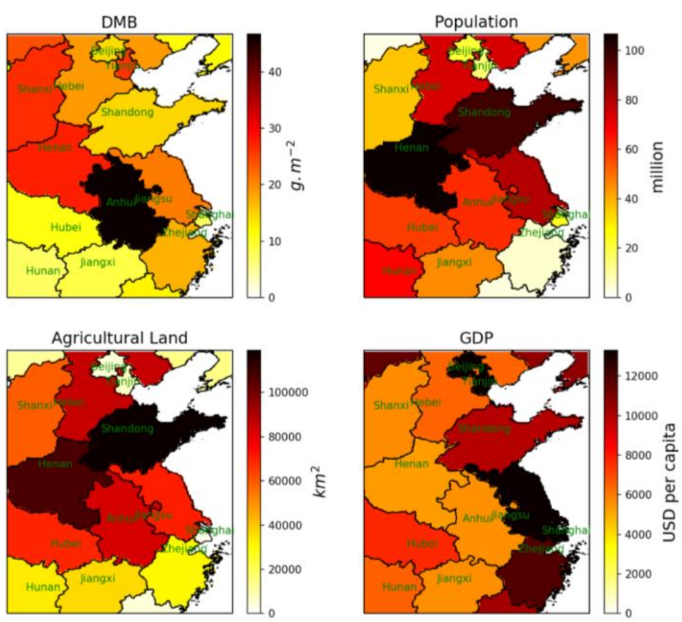

Figure 12: Spatial distribution of province-specific: (a) mean annual dry matter burned as calculated using the VIIRS-IM/Him approach developed herein, (b) population (Data source: Fu *et al.*, 2014a), (c) agricultural land area (Data source: GlobeLand30, http://www.globallandcover.com/) and (d) mean GDP per capita (Data source: Fu *et al.*, 2014b). The basic layer of country/province borders within this map was created using Python Basemap librabry.

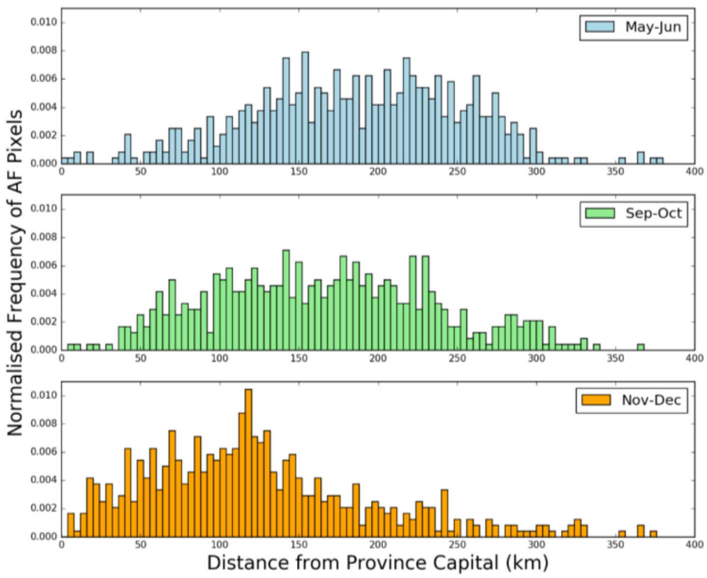

Figure 13: Normalised frequency distribution of distance from province capital of the top 10% of high FRE VIIRS-IM/Him product 0.1 degree grid cells during the three burning seasons: Summer - May to June (top, blue), Autumn – September to October (middle, green), and Winter - November to December (bottom, orange). A clear shift towards the origin can be observed in the Nov-Dec period compared with Sep-Oct.